THESIS FOR THE DEGREE OF LICENTIATE OF ENGINEERING

Operando X-Ray Imaging of Battery Electrodes

ANTOINE KLEIN

Department of Physics

CHALMERS UNIVERSITY OF TECHNOLOGY

Gothenburg, Sweden 2024

Operando X-Ray Imaging of Battery Electrodes
ANTOINE KLEIN

Department of Physics
Chalmers University of Technology
SE-412 96 Gothenburg
Sweden
Telephone + 46 (0)31-772 1000

Cover: 3D rendering of metallic deposition of lithium on a graphite electrode.

Chalmers Digitaltryck
Gothenburg, Sweden 2024

Operando X-Ray Imaging of Battery Electrodes

Antoine Klein
Department of Physics
Chalmers University of Technology

Abstract

Batteries are now part of our daily life as they enable easy usage of portable devices and are now essential for us to travel, communicate, work, read, or listen to music. The diversity of battery applications continuously increases and new demands of for instance capacity, charge time and sustainability have emerged. There is thus a need to either increase the understanding of existing technologies or develop new chemistries. At the core of a battery complex reactions are taking place at the electrodes, covering multiple length and time scales. This poses a great challenge to understand mechanisms and based on this develop new solutions. One way to tackle this challenge is to carry out *operando* experiments where properties or processes are investigated while the battery is being cycled.

This work focuses on *operando* analysis of three different battery systems, comprising both current lithium-ion batteries (LIBs) and next generation battery concepts, using X-ray imaging techniques. The key processes addressed are lithium plating, a classic degradation mechanism in LIBs batteries, the dissolution and reprecipitation of active material in lithium-sulfur batteries and the sodiation of hard carbon anodes for sodium-ion batteries. X-ray imaging allows to follow the processes in real time as well as image an extended volume of the electrode to correlate changes in morphology to the electrochemical processes taking place during cycling. From XTM experiments, we found that electrolyte composition affects the morphology of lithium plating at the graphite/separator interface and observed a change in the size distribution of sulfur particles after their redeposition at the end of the charge. Through S/WAXS tomography, we show the sodiation of a hard carbon anode spatial inhomogeneities.

Keywords: lithium-ion batteries, sodium-ion batteries, lithium-sulfur batteries, X-ray imaging, XTM, SAXS.

List of Papers

I Identifying the role of electrolyte additives for lithium plating on graphite electrode by operando X-ray tomography.
Antoine Klein, Matthew Sadd, Nataliia Mozhzhukhina, Martina Olsson, Ludovic Broche, Shizhao Xiong and Aleksandar Matic
Under review

II X-ray scattering imaging of sodiation of hard carbon anodes.
Martina Olsson, **Antoine Klein**, Nataliia Mozhzhukhina, Shizhao Xiong, Christian Appel, Mads Carlsen, Leonard Nielsen, Linnea Rensmo, Marianne Liebi, Aleksandar Matic
Manuscript

III Investigation of 3D structure evolution in lithium-sulfur batteries with computed X-ray tomography.
Antoine Klein, Salvatore de Angelis, Matthew Sadd, Stefano Checchia, Martina Olsson and Aleksandar Matic
Manuscript

Contribution Report

I I participated in the beamtime at the ID19 beamline at ESRF (Grenoble, France) which was performed with the co-authors. I performed all data analysis and wrote the first draft of the manuscript.

II I was part of the beamtime at the ID15a beamline at ESRF. Data reconstruction was performed by the co-authors, and I did all the data analysis and wrote the first draft of the manuscript.

III I participated in the planning of the S/WAXS experiment with the cell design and electrochemical testing of the capillary cell. I participated in the beamtime and contributed to the discussion of the results in the manuscript.

Table of Contents

1 Introduction

The constant economic growth of our modern society imposes an increased demand for energy. We use petrol, gas, and coal as if they are unlimited and consequenceless for the environment, but with the rarefication of fossil-fuel resources and their contribution to environmental pollution, our way of consuming excessively cannot remain as it is. Thus, a shift towards clean and sustainable ways to convert energy is necessary. One of the obstacles to developing non-carbonated energy systems is their intermittent nature (e.g., solar and wind power) but this can be tackled by combining them with an energy storage system. Lithium-ion batteries (LIBs), an established technology, could fulfil this role due to their high energy density [1,2]. From a more global point of view, applications of LIBs are diverse, from storage of intermittent renewable energy to portable devices and electric mobility. As a step towards limiting the impact of transportation on greenhouse gases, the European Union has agreed to a plan for the next decade to have "Zero emission from new cars by 2035" [3] which means that every new vehicle produced from then has to be electric. To meet this demand, an intense effort from the research community is needed to advance battery technology in terms of e.g., energy density, lifetime, rate capability and sustainability.

The key to reaching high performance in batteries is to understand the physical and electrochemical processes taking place at the core of the active materials. For example, a complete comprehension of degradation, storage mechanisms and ion transport are crucial questions in battery research. New technologies, unlike LIBs, have not benefited from half a century of extraordinary scientific research, and many intricate processes and mechanisms need to be understood. For instance, in sodium-ion batteries[4], common battery materials such as graphite cannot be used and instead hard carbons, with a more disordered structure, are a possible anode material but the storage mechanism still needs to be understood. Hard carbon is made of grains with micropores and a disordered, amorphous stack of graphene layers. A larger interlayer distance compared to graphite and the micropores make it possible to store of sodium ions. Similarly, the conversion reaction in lithium-sulfur batteries enables to considerably increase the energy density compared to LIBs but the complex conversion mechanism with dissolution and precipitation of sulfur lacks a clear comprehension to enable this technology the reach the market [5].

The scope of this thesis is to build a deep understanding of processes taking place inside a battery system through *operando* characterisation, i.e., while the battery is operating, with X-ray imaging. It enables to track physical processes in electrode materials to build a mechanistic understanding of the electrochemical processes. In Paper I, we investigated the effect of electrolyte additives on Li plating. Li-plating is a common degradation mechanism, occurring during abuse, low temperatures of fast-charging of a battery where metallic Li is deposited on the graphite electrode instead of intercalated. In Paper II, we tracked the sodiation of a hard carbon electrode in a custom capillary cell through *operando* S/WAXS tomography and observed micropore-filling inhomogeneities in the electrode. Finally, in Paper III, the morphological dissolution and precipitation of elemental sulfur were monitored and further characterised with particle analysis.

2 *Batteries*

2.1 Basic principles of batteries

A battery converts chemical energy to electric energy by the spontaneous reaction of an oxidant and a reducer. At discharge, the resulting current can be used to power a device and at charge, an external current is applied to reverse the reaction. At each electrode, an electrochemical half-reaction takes place.

Reduction:

$$O^{n+} + ne^- \rightarrow R \qquad \text{Eq. 1}$$

Oxidation:

$$R \rightarrow O^{n+} + ne^- \qquad \text{Eq. 2}$$

The electrode where the reduction occurs is called the cathode and the electrode where the oxidation happens is called the anode, O is the species accepting electrons and R is the one giving them. Electrodes are physically separated and an ion conductive medium, an electrolyte, transports the charged species via migration or diffusion. Each electrode reaction has an intrinsic potential given by the Gibbs free energy:

$$E = -\frac{\Delta G}{nF} \qquad \text{Eq. 3}$$

n being the number of electrons exchanged and *F* the Faraday constant and what is called the overall potential of the cell is defined by:

$$E_{cell} = E_{cathode} - E_{anode} \qquad \text{Eq. 4}$$

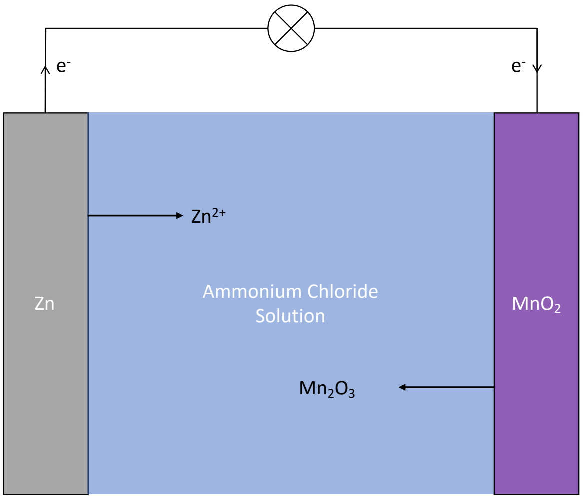

Figure 1. The basic scheme of a Leclanché cell, a precursor to the commonly used dry batteries [6].

Batteries are divided into two categories, the non-rechargeable (primary batteries) and rechargeable (secondary batteries, e.g., LIBs). An example of a primary battery, the Leclanché cell is shown in **Figure 1** where zinc is the reducer and manganese dioxide is the oxidant. The overall cell reaction is:

$$Zn + 2MnO_2 \leftrightarrow ZnO.Mn_2O_3 \qquad \text{Eq. 5}$$

The voltage cell is here 1.4 V and the cell is considered discharged when all the manganese dioxide was consumed and the end product hetaerolite $ZnO.Mn_2O_3$ formed [7].

Another important parameter of a battery is its capacity (in Ah) which is related to the number of electrons it can deliver:

$$C = \int I(t)dt \qquad \text{Eq. 6}$$

It is linked to the mass of reactants involved in the electrode reaction through Faraday's equation which gives the specific capacity of active materials:

$$C_s = \frac{nF}{M} \qquad \text{Eq. 7}$$

Here M is the molecular mass of the reactants, F is the Faraday's constant, and n is the number of electrons exchanged. The specific capacity is commonly expressed in mAh/g and defines how much charge a material can store. The energy output is often normalised by weight of active material, it is then called the energy density and expressed in Wh/kg:

$$W = E_{cell}\, C_S \qquad \text{Eq. 8}$$

From Eq. 8, one can understand that there are two ways to increase a battery's energy density, either by changing the cell voltage with a new combination of positive/negative electrode materials or by tuning the capacity with electrode composition.

2.2 Lithium-ion batteries

Lithium-ion batteries (LIBs) have become the state-of-the-art technology when it comes to secondary energy storage. They cover a wide range of applications, such as phones, laptops, and electric vehicles. Even though the first LIB was commercialised in 1991 by Sony [8], their working principle has not fundamentally changed since then. In a LIB, lithium ions are transported by a liquid electrolyte and inserted in the electrodes. The positive electrode is most commonly a lithiated transition metal oxide ($LiMO_x$) and the negative electrode is based on graphite.

Originally, positive electrode materials were layered sulfides, e.g., TiS_2, that could intercalate lithium ions at 2.5 V, as shown by Whittingham *et.al.* in the 70s [9]. Subsequently, Goodenough *et.al.* pushed the cell voltage to 4V by introducing lithium cobalt oxide (LCO) in a reversible way [10], while Yazami *et.al.* proved the possibility of reversibly intercalating Li^+ in graphitic materials [11], finally, Yoshino *et.al.* improved the electrolyte and safety [8]. In 2019, Whittingham, Goodenough and Yoshino received the Nobel Prize in chemistry "for the development of lithium-ion batteries" [12]. The first LIB introduced to the market by SONY only had an energy density of 80 Wh/kg, but this has, since then, been pushed to 250–300 Wh/kg with new types of active materials, electrolytes and engineering of the cell itself [13].

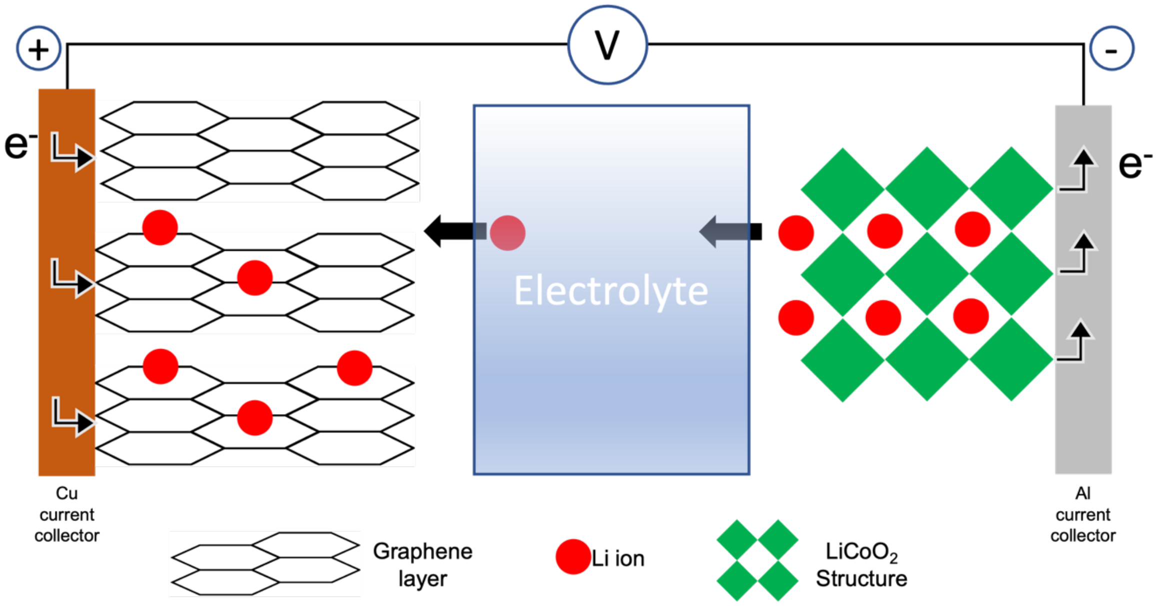

Figure 2. Schematic of a lithium-ion battery during charge.

Figure 2. shows the typical layout of a LIB. The usual negative electrode material is graphite which is a stack of graphene layers. Lithium ions intercalate at a potential between 0.2 and 0V vs. Li^+/Li thanks to the low van der Waals interaction between the graphene layers [14]. Graphite offers both high specific capacity (372 mAh/g), low electrode potential, and low cost (only made of carbon atoms), making it an excellent negative electrode material. On the cathode side, there is a variety of options to choose from depending on the desired application for the battery, e.g., if high energies or high power densities are desired. Transition metal oxides are the most common commercial positive electrode materials (e.g., $LiCoO_2$, $LiMn_2O_2$, $LiFePO_4$ or $LiNi_xMn_yCo_zO_2$), where lithium ions intercalate into available crystallographic sites. The electrolyte typically consists of the lithium salt $LiPF_6$ dissolved in a mixture of organic solvents [15] (e.g. Ethylene Carbonate (EC), Propylene Carbonate (PC) or Ethyl Methyl Carbonate (EMC)) in different ratios to improve the electrochemical and thermal stability window.

The voltage window at which LIBs are operating is essential to achieve a high energy density but at the same time, the electrolyte is not stable in this window. It will thus decompose at the electrode surface and this process is very important for stable cycling. The concept of a thin layer of decomposition products formed at the electrode/electrolyte interface was introduced by Peled in 1979 [16] and is called the Solid Electrolyte Interphase (SEI). It will prevent further electrolyte decomposition if the following conditions are met [17]:

- a good mechanical stability and adhesion to the electrode surface for it to not detach in case of swelling or cracking during cycling.
- to be electronically insulating to prevent further decomposition and a continuous consumption of the electrolyte.
- to be an ionic conductor to allow Li^+ diffusion to the electrode.
- homogenous in composition and distribution over the electrode to avoid preferred reaction sites.

The SEI is composed of various organic and inorganic compounds and their nature depends on the electrode, salt, solvent, and impurities in the electrolyte. Typical SEI products are LiF, Li_2O, Li_2CO_3, polyolefins and semi-carbonates [18]. When a battery is assembled, and the graphite electrode is immersed for the first time in the electrolyte it will spontaneously reduce and start to form a SEI. Additionally, SEI formation will take place during the initial cycles as the potential of the electrode decreases toward 0V vs. Li+/Li. Depending on the type of graphite, the current densities applied and the solvents and salt used, the SEI will be formed at different potential [18] and can be controlled by careful initial cycling at low current densities. This process is called precycling of the cell.

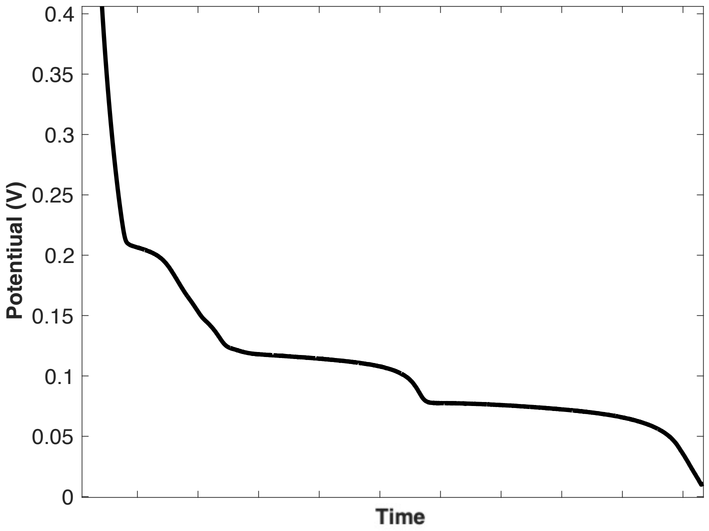

Figure 3. Voltage profile of a lithium-graphite stack in a coin cell during the intercalation process under constant current corresponding to a tenth of the total capacity (C/10, 0.18 mA). The steps correspond to an increased concentration of Li in graphite.

Graphite is a carbonaceous compound that is made of an ABAB stacking of hexagonal carbon layers (graphene). At low potential, lithium can intercalate between graphene planes typically at a potential below 0.2V vs. Li^+/Li (**Figure 3**). The overall intercalation reaction of Li in graphite can be summarised as:

$$xLi^+ + e^- + C_6 \rightarrow Li_xC_6 \; (0 < x < 1) \qquad \text{Eq. 9}$$

The different plateaus observed in the voltage profile correspond to the increased concentration of Li in Li_xC_6 ($0<x<1$) and represent the graphite layers being filled by lithium ions [19,20]. As lithium intercalates, the interlayer distance between graphene planes increases, resulting in an overall volume change of the bulk material and shift to an AAA stacking of graphene layers [21]. Different studies show that fully lithiated graphite swells about 10-13% in volume compared to its pristine state [20, 22, 23,24].

2.2.1 Lithium plating

Lithium plating is a common degradation mechanism during the lithiation of graphite [25]. As lithium ions are intercalated in graphite, the potential of the electrode drops close to 0 V vs. Li^+/Li (**Figure 3**). Theoretically, the intercalation reaction should stop at this limit but under high current densities, high state of charge (SOC) or low-temperature conditions [25], the potential can drop below 0 V and trigger lithium metal deposition instead of insertion. In addition, if graphite is already fully lithiated (i.e., in case of a high state of charge or overcharging), there is no more space in the electrode to accommodate Li^+ which will result in an accumulation of ions at the electrode-electrolyte interface and lithium can plate and form a metallic film at the surface of graphite. The SOC dependence of plating was studied by Petzl et.al. who proposed a linear relationship between the mass of deposited lithium and SOC [13].

Charging at low temperatures increases the risk of lithium plating, typically, in the temperature range is -20°C to + 60°C [28]. It is considered that below -20°C, transport proprieties, like diffusion of lithium in graphite, ionic conductivity (in the electrolyte and SEI), and charge transfer rate are significantly decreased [27] and at low temperatures, lithium ions adsorb at the graphite interface faster than they can diffuse into the electrode, resulting in an accumulation of charges and thus a rise for onset of lithium plating [29]

There are two main effects on the battery when lithium plating occurs: one is a safety issue and the other is a capacity fade. Plated lithium typically grows in a dendritic fashion [30] e.g., in tall, spiky structures that can lead to short circuits of the cell if they reach the positive electrode. The short circuit causes a rapid and uncontrolled increase in temperature (also called thermal runaway) to the point where the battery fails catastrophically and releases all its energy in the form of heat [31]. The capacity fade over multiple cycles due to Li-plating is caused by different phenomena [27]. The first one is the loss of active material with the creation of dead Li. After lithium has been plated, a fraction of it will be stripped back during the discharge, it is thus called reversible lithium plating and does not lead to capacity fade. If part of the plated lithium is not stripped back it is simply not available anymore which causes a loss of lithium inventory and thus available capacity [32]. The plating and growth of lithium also lead to new surfaces available for the formation of fresh SEI [33] and the electronically insulating nature of SEI can lead to the disconnection of dendrites from the electrode, creating dead Li. As seen in section 2.2, SEI is made of various components from the electrolyte. This newly formed SEI causes a continuous consumption of electrolyte, leading to further capacity fade [27].

The electrolyte plays a major role for Li plating and choosing the right combination of salt solvent and additives can help to tackle issues in LIB. For instance, the introduction of small concentrations of additional species in the electrolyte is a strategy to mitigate Li plating, by forming different SEI. For instance, Jones *et.al.* showed the beneficial effect of lithium bis(fluorosulfonyl)imide (LiFSI) on lithium plating at low temperatures (down to -50 °C) [34]. This improvement was due to a reduced SEI resistance while also not altering kinetics at the positive electrode. They also claimed that the addition of vinylene carbonate (VC) resulted in a tendency for lithium plating at low temperatures compared to a baseline electrolyte composed EC, EMC, and methyl propionate (MP) in a 20:20:60 volume ratio with 1.0 M LiPF6. On the other hand, it was shown by Burns *et.al.* that VC can have a beneficial effect on plating [35] depending on its concentration. LiFSI and VC are SEI modifier additives that create different SEI compositions. VC decomposes at the graphite/electrolyte interface into a polymeric thin film, protecting from further electrolyte composition [36]. LiFSI acts differently by creating a SEI rich in inorganic lithium compounds, such as LiF [37,38].

2.2.2 Detection of lithium plating

The detection of lithium plating in LIBs is often considered a challenging task, especially in commercial cells. The theoretical definition of the start of Li plating is the electrode potential dropping below 0V vs. Li^+/Li. However, this simple condition is most often hard to verify since the overall cell voltage is measured by the difference in potential between the two electrodes in the cell. Thus, knowing the actual potential of one of the electrodes is impossible in this setup. To address this issue, one can introduce a third reference electrode, enabling one to determine the potential of the individual electrodes. This simple and reliable method can detect Li plating but its implementation in battery cells requires design modifications that can impact battery performance [39,40]. Another method that can be implemented in an operating battery is the analysis of differential capacity during delithiation. In this step, plated lithium will be stripped first, i.e. at a voltage lower than the de-intercalation process, and can be observed in the voltage profile by an early plateau [41]. Differential capacity analysis can exacerbate this high voltage plateau during delithiation by transforming it into a peak, allowing an easy identification of the lithium plating onset [34,42]. This method can easily be applied while the battery is being cycled but needs to have control cycles with minimal current densities to avoid the overlap of de-intercalation reaction and Li-stripping in the voltage profile.

To identify plated Li after the battery has been cycled, it is possible to open the cell and visually inspect the electrode. This method has the advantage of being simple but destructive and not quantitative [43]. Observation of lithium deposition can also be done by various surface techniques e.g., Atomic Force Microscopy (AFM) [44], Transmission Electron Microscopy (TEM) [45] or optical microscopy [30], [46]. These methods can image the electrode and identify plated Li. However, they cannot provide a quantitative analysis of the deposition which is crucial to be able to compare studies and carry out deeper analysis. Nuclear Magnetic Resonance (NMR) has a great sensitivity of ^7Li, resulting in short measurement times. and can not only quantify the mass of plated Li but also determine the type of plated morphology whether it is mossy or dendritic [47,48].

Raman spectroscopy has also been used to identify plated Li [49,50]. Metallic deposition has a signature in the Raman spectrum when it forms a new bond in the SEI on graphite during nucleation. This new bond results in a Raman band around 1850 cm^{-1}, is characteristic of lithium acetylide species (Li_2C_2) and can be used to locate specific spots where lithium plating occurs on the electrode. In **Figure 4**, an optical microscopy image shows in which regions Raman spectra have been resolved. The gold-looking 'Region 1' is a lithiated graphite grain and displays the typical Raman G-band at around 1600 cm^{-1}. In 'Region 2', one can identify a grey-looking phase associated with lithium plating. The spectrum in this region shows a band at 1853 cm^{-1} which is not present in 'Region 1'.

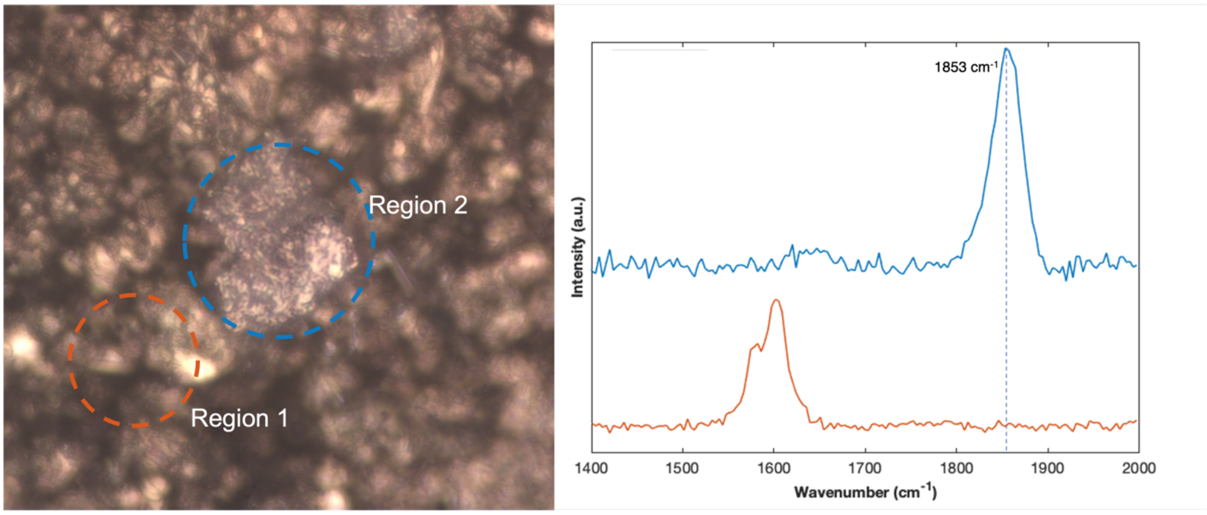

Figure 4. Optical microscopy image of a fully lithiated graphite electrode surface and associated Raman spectra. The electrode comes from a cycled coin cell and is put in an air-tight cell with a glass window, enabling Raman imaging of the electrode.

X-ray imaging has been used to track lithium formation on various substrates [22,51,52,53]. X-ray tomography microscopy can provide a 3D image of lithium microstructure while the battery is being cycled. However, identifying lithium growing on a graphite surface is challenging in absorption-based tomography because of the poor contrast between graphite, electrolyte-filled pores and deposited Li [54].

2.3 Lithium-sulfur batteries

Lithium-sulfur (Li/S) is a promising next-generation battery chemistry to replace the current state-of-the-art LIBs. The large specific capacity of elemental sulfur (1672mAh/g) compared to common positive electrode materials (140mAh/g for $LiCoO_2$), the non-toxicity and the abundance of sulfur makes it a suitable choice for sustainable, high energy batteries [5,55]. A Li/S battery is generally made up of elemental sulfur, S_8, embedded in a matrix of conductive carbon and a binder. The binder ensures that the composite electrode holds together, and the carbon additive creates an electron-conductive network to electrically connect sulfur particles as sulfur is an insulator (scheme in **Figure 5a**). The capacity of the cell comes from the conversion of elemental sulfur to Li_2S according to:

$$S + 2Li^{+} + 2e^{-} \rightarrow Li_2S \qquad \text{Eq. 10}$$

However, the conversion reaction itself can be broken down into several steps [56]:

$$S_8 + 2Li^+ + 2e^- \rightarrow Li_2S_8 \qquad \text{Eq. 11}$$

$$Li_2S_8 + 2Li^+ + 2e^- \rightarrow Li_2S_{8-n} + Li_2S_n\ (n = 4 - 6) \qquad \text{Eq. 12}$$

$$Li_2S_{8-n} + Li_2S_n + 12Li^+ + 12e^- \rightarrow 8Li_2S \qquad \text{Eq. 13}$$

At the beginning of the discharge, elemental solid sulfur, S_8, converts to the polysulfide Li_2S_8 according to Eq. 11. In common electrolytes, this product is soluble so the initial reaction also involves a solid-liquid transition which is related to a plateau in voltage profile (**Figure 5b**) between 2.3-2.4V[57], [58], [59]. Subsequently, long-chain polysulfides are converted to shorter-chain polysulfides Li_2S_n (n = 4 – 6) in a liquid-liquid reaction (Eq. 12), since these polysulfides are all soluble in common electrolyte. This is represented in the voltage profile by the slope between the first high-voltage plateau and a second plateau around 2.1V. This lower plateau represents further conversion of Li_2S_n to the end product Li_2S. The last step also involves a liquid-to-solid transition since Li_2S is insoluble in most common electrolytes. The cell polarisation at the very end of the discharge (a fast drop of the potential) indicates that all the sulfur has been converted to Li_2S and the reaction is terminated.

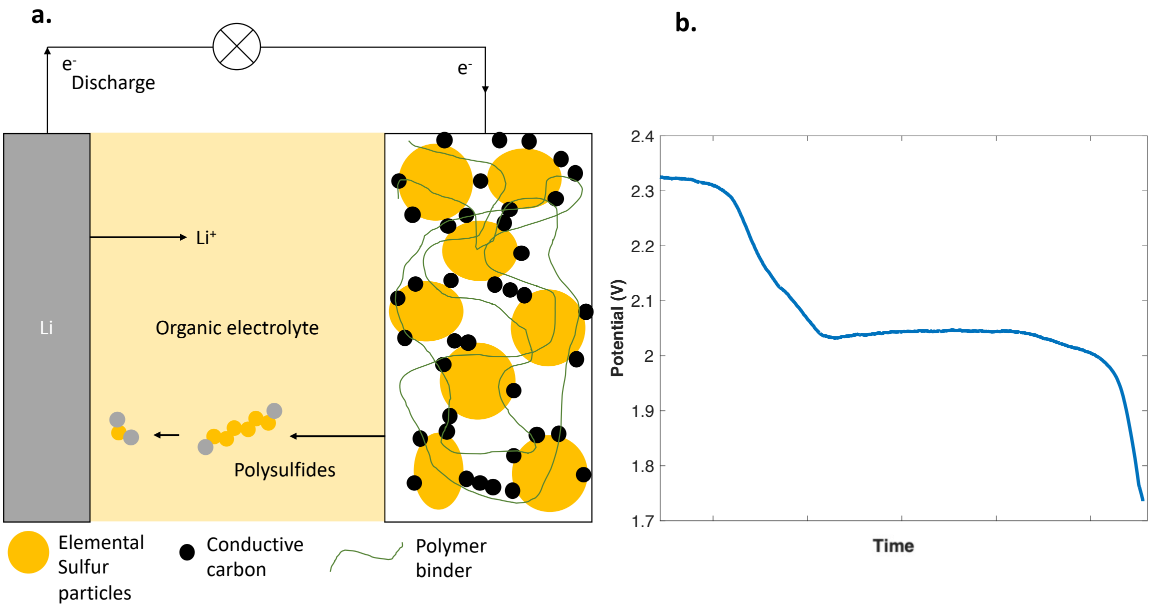

Figure 5. a. Scheme of a Li/S cell with a sulfur-carbon composite electrode combined with a Li metal counter-electrode. b. Voltage profile of a Li/S cell at discharge under a constant current of 1C corresponding to 3.4 mA/cm^2.

Since intermediate conversion products, Li_2S_n (n = 3 – 8), are soluble in the liquid electrolyte, they can diffuse due to concentration gradients in the electrolyte towards the counter electrode. Once at the Li surface and during the charge, they can gain an electron and reduce to shorter chains and then, they diffuse back to the working electrode where they are oxidised once again. This reaction is known as the shuttle effect and is a parasitic reaction responsible for the poor coulombic efficiency of many Li/S batteries [60, 61,62]. Another issue connected to the solubility of polysulfides is that diffusion back to the cathode can be slow. This leads to capacity fade during cycling as a part of the active material is lost in the electrolyte [5]. Another important aspect of Li/S batteries is the electrolyte/sulfur ratio (E/S) which needs to be as low as possible (≈1 μL/mg) to reach high energy densities [63]. However, at the research scale, the E/S ratio is often reported to be >20 μL/mg [64]. This gives a false representation of cell performances since a flooded cell can compensate for the loss of sulfur due to diffusion and shuttle effects.

The solid-liquid-solid reaction described by Eq. 11-13 is valid for the common ether-based electrolytes [59]. They are typically composed of the lithium bis(trifluoromethanesulfonyl)imide (LiTFSI) salt in a mix of two solvents: 1,2dimethoxyethane (DME) and 1,3-dioxolane (DOL) in a 1:1 volume ratio. Lithium nitrate ($LiNO_3$) is added to form a stable SEI at the Li-metal anode and mitigate the shuttle effect [63]. To circumvent polysulfide dissolution and loss of active material, another reaction pathway can be followed, where elemental sulfur is directly converted to short-chain polysulfides with a lower solubility compared to longer ones, called the quasi-solid reaction pathway [59]. This type of reaction is enabled using different solvents (usually with a higher viscosity) that prevent dissolution. One example is the system developed by the Nazar group which is a glyme-based [64], and another electrolyte from CIC, energiGUNE is based on sulfolane and a highly fluorinated ether-based solvent [65]. In these studies, a low electrolyte to sulfur ratio was used and still resulted in high specific capacities, i.e. high active material utilisation.

A massive research effort is needed to understand the complex sulfur conversion reaction and improve Li/S cells. Characterisation techniques such as the X-Ray Diffraction (XRD) [58] showed that polysulfides adsorb on the fibres of a glass fibre separator, identifying their diffraction peaks thanks to their interaction with silica. Raman spectroscopy, [66] has been used to provide a better comprehension of polysulfide evolution in the electrolyte with selective solubility of fluorinated ether-based electrolytes. X-ray tomographic microscopy (XTM) has been used to directly image sulfur particles and quantify their dissolution/precipitation throughout cycling [57,67,68,69]. Tan *et. al.* used absorption-based computed tomography to resolve a sulfur cathode and reported that the reaction rate is diffusion-limited since the dissolution and precipitation of elemental sulfur evolves from the cathode-separator interface [68]. More recently, Sadd *et.al.* applied synchrotron-based XTM to demonstrate the complete dissolution of sulfur and observe the precipitation of end-of-discharge product Li_2S with a phase contrast reconstruction [57].

2.4 Sodium-ion intercalation in hard carbon

Sodium-ion Batteries (NIBs) are an alternative to LIBs with the promise to improve sustainability, sodium is the 4th most abundant element in Earth's crust [70]. However, unlike lithium, graphite is not suited for NIBs since the intercalation of sodium into graphite is limited [71]. Hence, an alternative of high-performance anode is needed. Other types of carbonaceous materials have instead been investigated for NIBs [71]. Among them, hard carbons (HC) are a promising class of negative electrode materials with high specific capacity. For instance, Zhao *et. al.* combined a 400 mAh/g HC anode with a layered oxide positive electrode to make a cell with an energy density of 240Wh/kg based on the materials used [68].

Hard carbons are disordered materials and lack the long-range order of graphite. HC particles contain both open and closed nano-sized pores, granting them superior mechanical strength compared to graphite, hence the term hard carbon [71,74] (**Figure 6a**). Moreover, the graphene layers in HC are randomly stacked and oriented compared to the regularly oriented and spaced layers in graphite (**Figure 6b)**. HC is synthesised by pyrolysis of various organic precursors below the graphitization temperature of 3000°C [72], and the specific synthesis temperature will influence both the pore size distribution and graphene spacing [75]. Typical pyrolysis temperature range is between 1000°C and 2000°C, giving a pore size distribution of 5.1 Å to 9.2 Å in radius [74].

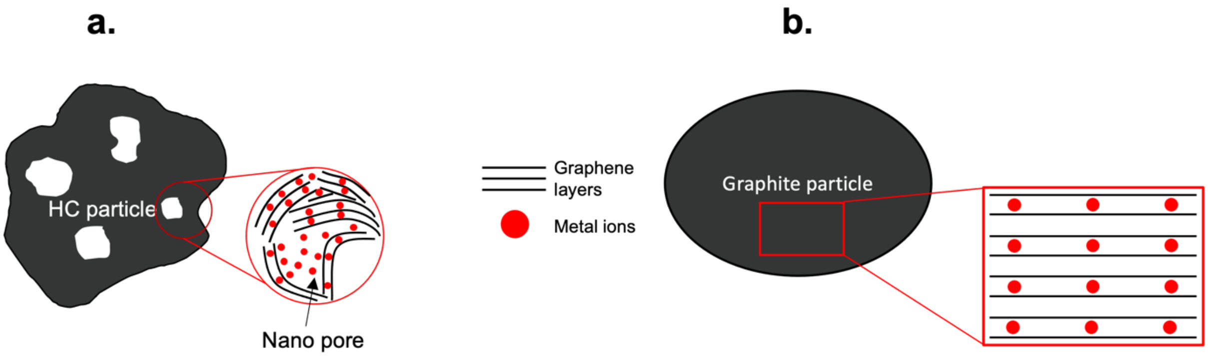

Figure 6. Comparison between a. Graphite and b. hard carbon structures. The schematics and zoomed inset are not to scale.

The extra space in the pores and between graphene layers enables new ways for ion insertion, leading to a more complex storage mechanism with both pore filling and intercalation between graphene layers and the sodiation mechanism is still up to debate [72]. A typical voltage profile of HC sodiation is shown in **Figure 7**. Generally, the slope region is attributed to intercalation between graphene layers and the plateau region to pore filling [72], [74]. However, HC structure can vary considerably depending on the pyrolysis temperature and precursor which complicates the creation of a single model to fully describe the storage mechanism. High pyrolysis temperature means that the HC structure is closer to a highly ordered long-range structure of graphite. It is expected that elevated synthesis temperature (typically at 2000°C), reduce defect concentration and interlayer spacing, as well as increase the nanopore size distribution in the hard carbon structure [74], [75].

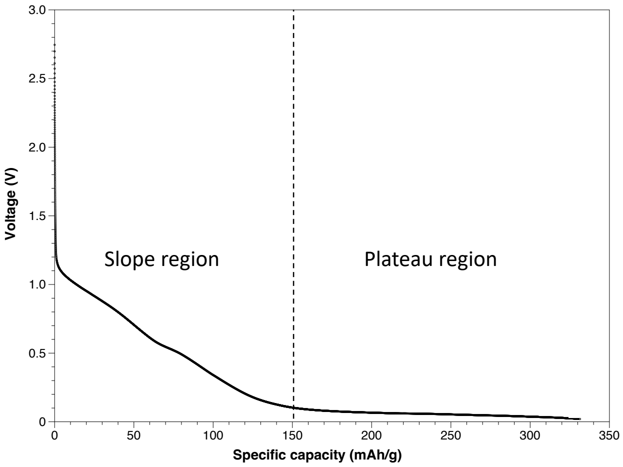

Figure 7. Voltage profile of the sodiation of commercial hard carbon at a constant current of an HC–Na coin cell. The current corresponds to a tenth of the capacity (20 mA/g)

Studying the sodiation process is a challenging task due to the complex structure of hard carbons. However, scattering techniques are well suited to understand how sodium is inserted in HC. For instance, with Raman scattering, the effect of the pyrolysis temperature on the HC structure has been investigated. The HC Raman spectrum shows the characteristic D (≈1350 cm^{-1}) and G bands (≈1590 cm^{-1}), related to sp^2 carbon atoms bond stretching and breathing, respectively. The intensity ratio of these two bands can be used as an estimation of the defect concentration in HC (e.g., vacancy point defects) [74]. Small and wide-angle X-ray scattering (S/WAXS) are particularly useful to describe the HC structure. By modelling the SAXS pattern [74,76], it is possible to extract information on particle roughness and nanopore size evolution during the sodiation process. The WAXS curve can be modelled by pseudo-Voigt functions [75] to determine the crystallinity, interlayer and in-plane spacing but also to identify the onset of side reactions such as sodium plating. A S/WAXS pattern showing different features of hard carbon is discussed later in this thesis.

3 *Experimental methods*

3.1 Electrochemical characterisation

Galvanostatic cycling is a common battery method to both understand reaction mechanisms and evaluate cell performance. In this technique, a constant current is applied and the potential response between the two electrodes is measured, and it is possible to extract useful cell parameters such as its capacity, coulombic efficiency ($\text{capacity}_{\text{charge}}$ / $\text{capacity}_{\text{disharge}}$) or rate capability. The choice of the current is usually made with respect to the mass of one of the electrodes (mA/g) or its area (mA/cm^2)

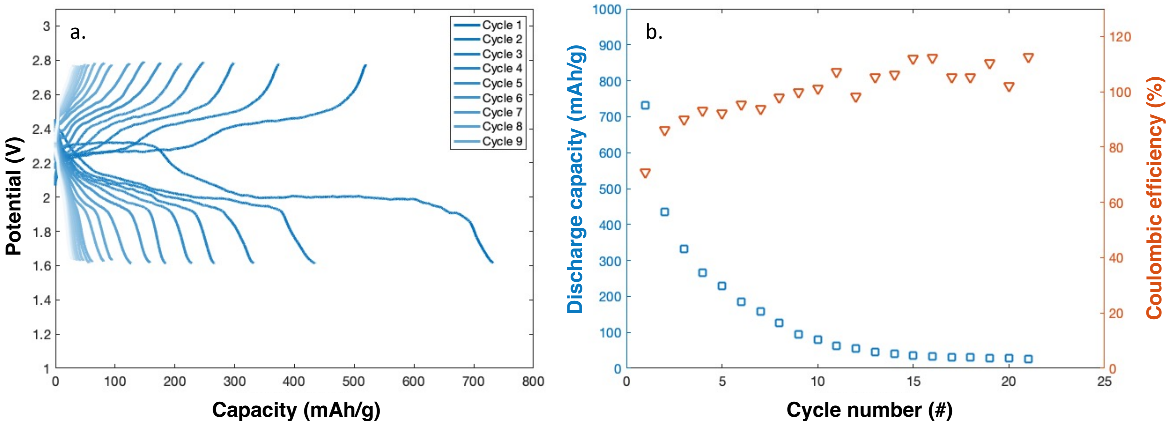

Figure 8. a. Galvanostatic cycling of a Li/S cell over multiple cycles at a current of 1C which corresponds to 3.4 mA/cm^2 in this cell and b. the corresponding discharge capacity and coulombic efficiency.

Figure 8a shows the voltage profile of the charge and discharge of a Li/S cell where elemental sulfur is the positive electrode and Li metal is the negative electrode. The x-axis is given as the specific capacity (mAh/g) instead of time to be able to compare different active materials or charge/discharge rates. The capacity fade over multiple cycles can be observed in **Figure 8b** as well as the coulombic efficiency.

In a "half-cell" configuration, the negative electrode is a metallic Li foil and has the function of being a large reservoir of lithium. The main advantage of a half-cell configuration is that despite having a two-electrodes set up, we can assume that the potential of the metallic counter electrode is close to 0V vs. M^+/M (M=Li, Na, K, Mg, or Zn) since the reaction taking place is the plating or stripping of the metal. Therefore, the overall potential of the cell can be assumed to be the one of the working electrode. A "full-cell" uses an actual active material at both positive and negative electrodes. The battery is being tested in conditions closer to a commercial cell to evaluate its performance. **Figure 9** shows the voltage profile of a cell with $LiFePO_4$ (LFP) as the positive electrode and graphite as the negative electrode. The overall voltage is the combination of graphite/LFP intercalation/deintercalation processes at both electrodes. With **Figure 8** and **Figure 9**, we can compare sulfur and LFP as positive electrode materials, where LFP shows better cycling stability (over 10 cycles) but has a lower specific capacity for the same current rate (at 1C). However, the actual current density (in mA/cm^2) was higher for the Li/S cell.

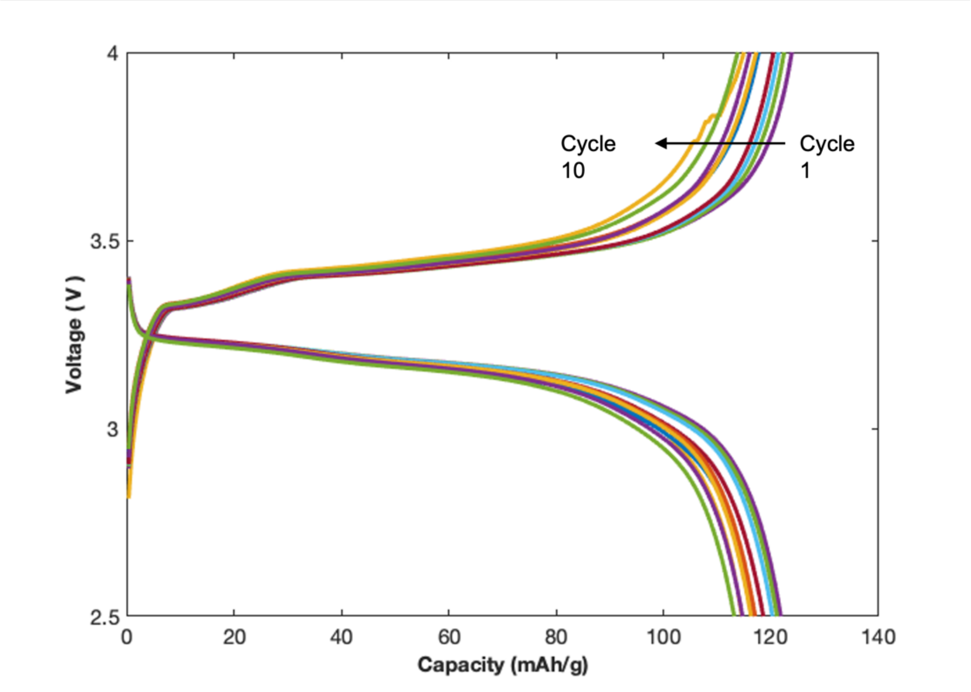

Figure 9. Voltage profile of $LiFePO_4$–Graphite full-cell over 10 cycles at a current of 1C corresponding to 2.0 mAh/cm^2.

3.1.1 Coin cell design

At the lab scale, the most common cell used to test battery materials is the coin cell. It allows rapid and easy cell assembly and material screening before any test in a larger cell format (e.g., pouch cell or cylindrical cell). The components of a coin cell are shown in **Figure 10**.

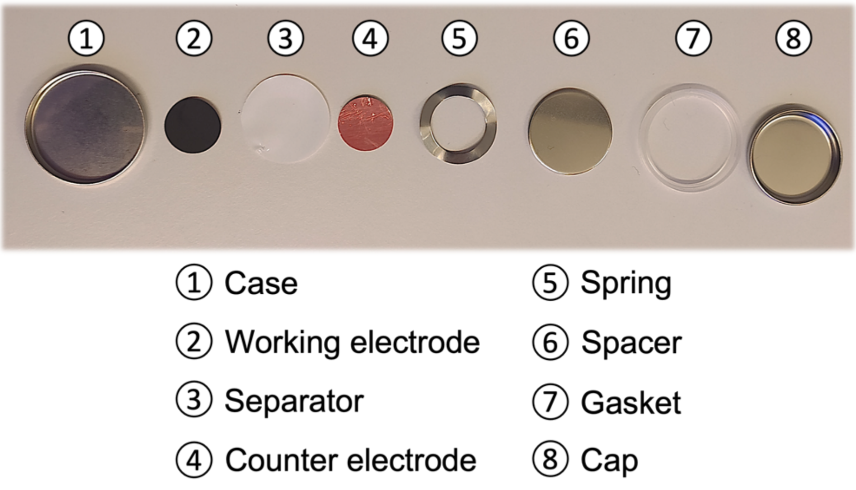

Figure 10. Photograph of the different coin cell parts.

However, a coin cell design is not always adapted for materials characterisation techniques to be performed in-situ or *operando*. The stainless-steel casing that makes the coin cell prevents access to visible light which makes Raman spectroscopy or optical microscopy experiments impossible to perform without heavy cell modifications (e.g., drilling a hole and putting a window). X-rays can be used to perform scattering experiments but only at high enough energies, e.g., Finegan *et.al.* performed *operando* X-Ray Diffraction (XRD) to monitor graphite intercalation using a coin cell with a 72.1 keV monochromatic beam [77]. Other types of cells suited for in-situ or *operando* will be discussed later in this thesis.

3.1.2 PEEK cell design

Other cell designs based on materials that are more X-ray transparent and stable against the electrolyte are required to achieve good image data quality. However, the cell still needs also to have good electrochemical performances to have results relevant results compared to classical cells (e.g., coin cell, Swagelok cell or pouch cell) for X-ray imaging.

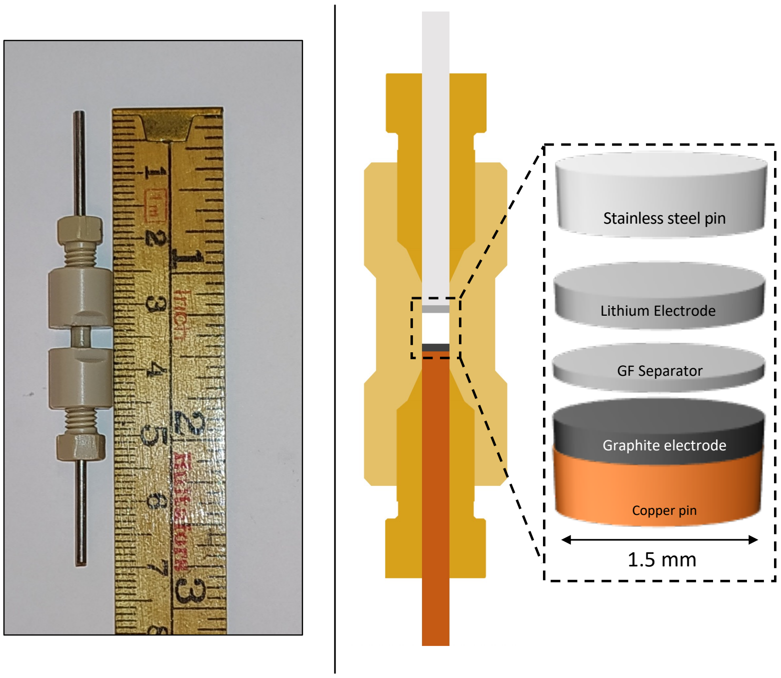

Figure 11. Photograph and scheme of the tomography cell used for XTM experiments. A blow-up view of the battery stack shows the graphite-lithium half-cell configuration.

In the experiment carried out at the ID19 beamline at the European Synchrotron Radiation Facilities (ESRF) a cell made of Polyether Ether Ketone (PEEK) with an internal diameter of 1.5 mm (**Figure 11**) was used. PEEK has a high X-ray transmission and is suitable as battery because of its good chemical stability. The middle section of the cell (where the electrode stack is located) was further cut to reduce X-ray attenuation. The pressure applied between the two electrodes is made by two metal plungers (used as current collectors) held in place by ferrules and screws that ensure the airtightness of the cell. The FOV achieved with the camera is 1.48 x 1.48 mm^2 and with an electrode diameter of 1.5 mm, 97 % of the electrode surface can be captured.

3.1.3 Capillary cell design

For S/WAXS experiment, PEEK is not well suited as it has a strong scattering signal [78] which may overlap with the features of interest. To circumvent this issue, a quartz capillary cell design can be used. The cell is shown in **Figure 12**.

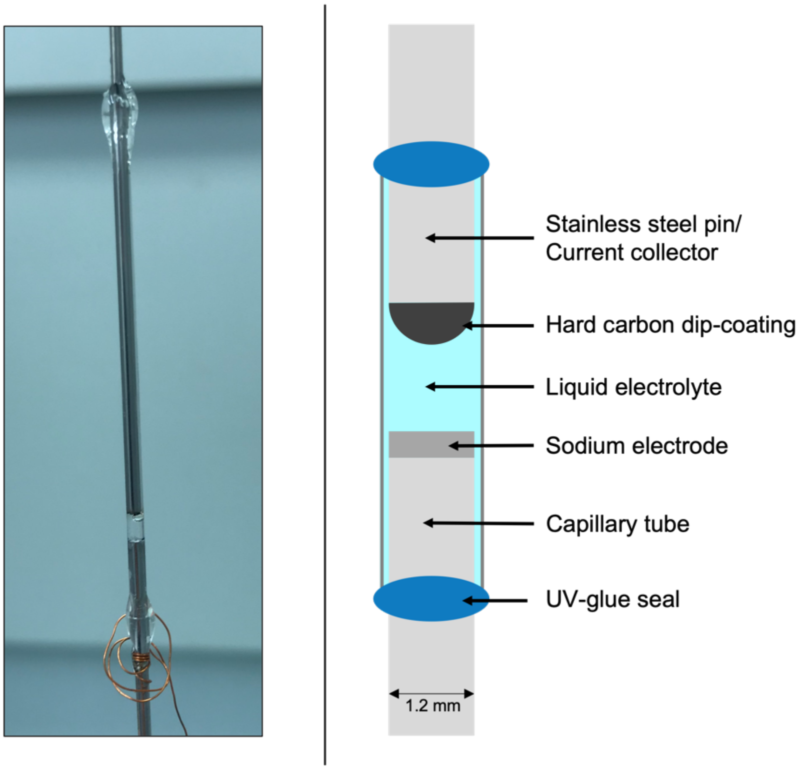

Figure 12. Photograph of a capillary cell for SAXS experiments and schematic with the different components indicated. Copper wires soldered at the bottom and top (not shown) ensure electrical connection.

The hard carbon dip-coated electrode is made from a slurry made of 85 wt.% HC, 10 wt.% PVDF binder and 5 wt.% carbon additives and inserted in the glass capillary tube. Then the capillary is filled with electrolyte and the other pin with sodium metal is inserted. The cell is air-tight and sealed with a UV-curable glue.

The small pin diameter (in the range of 0.8 to 1.2 mm) enables to capture the entire electrode in the FOV and analysis of the full electrode to observe inhomogeneities in the sodiation over the HC anode. Another advantage of the capillary cell is that the transparent glass, with no separator, allows direct observation of the electrode and electrolyte, meaning that quantitative analysis based on optical imaging can be carried out [57].

The main issue of this cell design is that is extremely fragile, meaning that its assembly procedure is challenging and requires careful handling of the quartz tube. It is also difficult to precisely control the distance between the electrodes which leads to a cell that cannot be reproduced exactly. Additionally, gas can be trapped between the pin and the capillary wall when assembling the cell. It can eventually move when handling the cell or simply by gravity move in the space filled by electrolyte between the electrodes (see the photograph in **Figure 12**). This can severely reduce the cell performance or even lead to the cell failure if the bubble grows too big. Finally, the electrode slurry is dip-coated on the pin which makes it difficult to know the electrode's actual capacity with great precision. The capacity can be determined before cycling by segmentation of the electrode with an initial XTM scan.

3.2 Small Angle X-ray Scattering

Small Angle X-ray Scattering (SAXS) is a characterisation technique based on the elastic scattering of X-rays with matter. SAXS is sensitive to structural change such as the average particles and shape distribution of a material, but it can also address its crystallinity and ordering. This non-invasive technique has diverse applications (e.g., powder dispersion, polymers, metals, porous materials) and can give information about materials at length scales in the nanometer range.

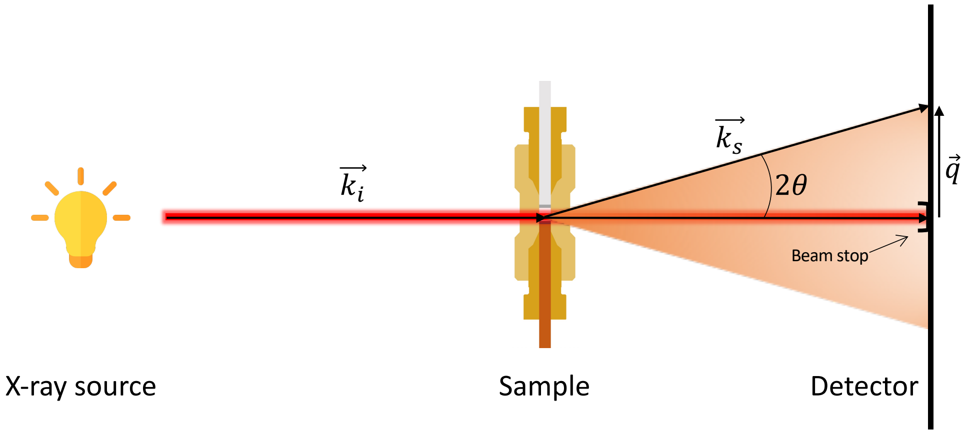

Figure 13. Schematic of a SAXS setup. The large sample-to-detector distance (2-50m) allows scattering at low angles, giving structural information on nanometre length scales.

A typical SAXS setup is shown in **Figure 13** where an incident monochromatic X-ray beam, defined by the wave vector $\overrightarrow{k_\iota}$ impinges on the sample and is elastically scattered at the angle 2θ. The scattered beam is represented by the wave vector $\overrightarrow{k_s}$. From this, it is possible to define the scattering vector $\vec{q}$:

$$q = \left|\overrightarrow{k_s} - \overrightarrow{k_\iota}\right| = \frac{4\pi}{\lambda}\sin\theta \qquad \text{Eq. 14}$$

where λ is the X-ray wavelength and θ is half of the scattering angle. Using q instead of the scattering angle is convenient since it allows for a direct comparison between scattering patterns, independently of the source wavelength. The vector $\vec{q}$ represents the structure length scale in reciprocal space and gives an idea of the size of objects scattered by the beam.

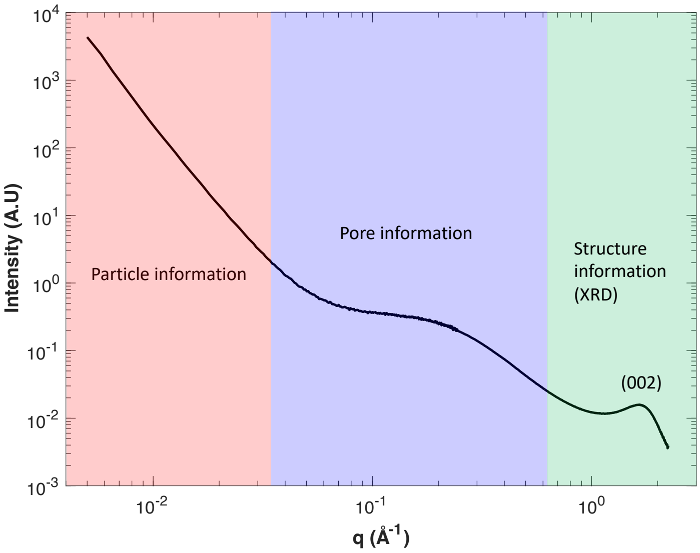

Figure 14. SAXS curve from a hard carbon powder on loglog scale. Low q values (red) are the contribution of the particles, the medium q range (blue) contains information on the nanopores, and the high q region (green) is the wide-angle X-ray scattering (WAXS) range with crystal structure information.

As an example, a typical SAXS pattern from a hard carbon powder is shown in **Figure 14** with a power law dependence at low q, a shoulder or bump at intermediate q and a peak at high q corresponding to the (002) reflection of graphite planes. To extract quantitative information, the SAXS curve needs to be modelled or fitted. There are multiple models to fit the SAXS curve from hard carbons, e.g., the Porod slope at low q which describes the particle roughness [71, 74].

By using a focused beam, it is possible to spatially scan the sample and get SAXS patterns at multiple points across the sample [79]. In this way, a SAXS image can be obtained with each beam position corresponding to a pixel that contains the full scattering pattern. The spatial resolution of the SAXS image depends on the beam step size. This mode of data acquisition is called scanning SAXS as opposed to full-field imaging where the entire sample is illuminated. Scanning SAXS allow to build 2D images of the sample and plots scattering intensities from each pixel at a certain q range for example. Full-field tomography can be achieved by a sample rotation of 180° and producing spatially resolved 3D images.

3.3 X-ray Tomographic Microscopy

X-ray Tomographic Microscopy (XTM) is a particularly powerful method to access the bulk of material and get detailed 3D information on micrometre length scales. It is common to perform XTM at synchrotron radiation facilities because of a high flux enabling to collect high-quality data. Additionally, in a synchrotron-based experiment, it is easy to tune the beam energy (in the range of 1 keV to 100 keV) and use a monochromatic beam to reach high contrast and spatial resolution.

Synchrotron-based XTM has been extensively used to study LIBs and has a variety of applications, giving a deep comprehension of phenomena in batteries. For instance, degradation mechanisms like thermal runaway and Li-plating can be studied and quantified with XTM [22,80]. Another application of XTM to battery research is the understanding of the the growth of lithium microstructures [51] or the evolution of individual particles in the bulk cathode [81]. The spatial resolution achieved in synchrotron-based XTM can range from 100 nm in nano-tomography [81] to a few micrometres in full-field XTM [80].

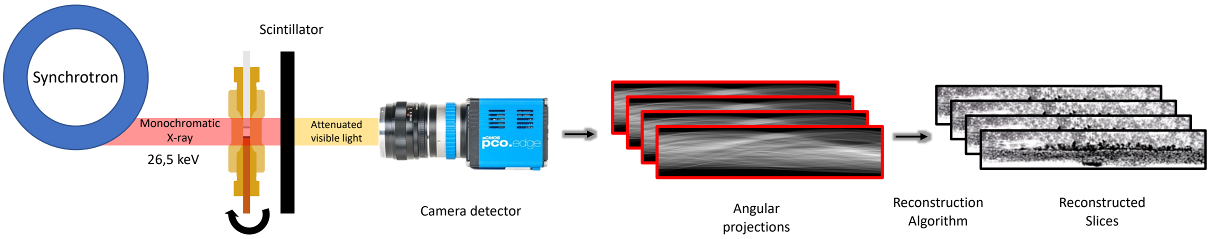

Figure 15. Schematic of a XTM experiment at a synchrotron with initial data reconstruction steps.

A typical layout for a XTM experiment is shown in **Figure 15**. The monochromatic X-ray beam illuminates the sample mounted on a rotation stage. The transmitted signal is converted to visible light and is captured by a camera detector to produce raw radiographs. These radiographs taken at different angles make a set of angular projections that are computationally reconstructed to form 3D images. The transmitted signal is attenuated by the sample according to the Beer-Lambert law's equation:

$$I = I_0 e^{-\mu d} \quad \text{Eq. 15}$$

where I is the transmitted beam intensity, I_0 is the intensity of the incoming beam, d is the thickness of the material and μ the absorption coefficient. The whole goal of XTM is to get the μ coefficient since it is linked to the electron density of a material with the following equation:

$$\mu = \frac{\rho Z^4}{AE^3} \quad \text{Eq. 16}$$

where ρ is the density, Z is the atomic number, A is the atomic mass and E is the X-ray energy. We can understand from Eq. 16 that when designing an XTM experiment, one must also carefully choose the beam energy to obtain a good contrast between the materials in the investigated object.

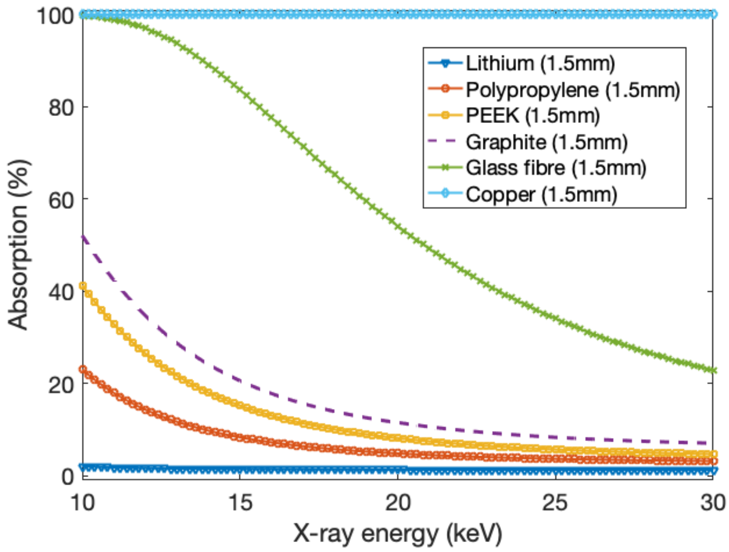

Figure 16. Calculated absorption as a function of X-ray energy of different cell components in a Li/graphite cell. The calculation has been made by using the website of the Centre for X-ray Optics at Lawrence Berkeley National Laboratory: https://henke.lbl.gov/optical_constants/filter2.html [82]

Figure 16 shows the simulated transmission of Li-metal/graphite cell with a glass fibre separator and copper current collector as a function of X-energy. The thickness used in the simulation is typical for the diameter of a cell used for tomography (see **Figure 11**). Copper almost fully absorbs all the X-rays and can potentially shadow materials situated between it and the detector and in contrast, lithium is X-ray transparent. The separator made of glass fibre could potentially be an issue considering its high absorption, but it can also bring a good contrast to the materials of interest (graphite, lithium). If the energy is too low, the transmitted beam will be attenuated too much and if the energy is too high, the contrast between the materials in the cell will be poor. Looking at absorption of the different materials in the cell (**Figure 16**) a suitable beam energy range can be 25-30 keV. An important aspect to consider is also the potential damage that the beam can cause to the sample. The battery electrolyte can, for instance, break down and form gas if the X-ray energy is set too low and/or with a dose too high [54].

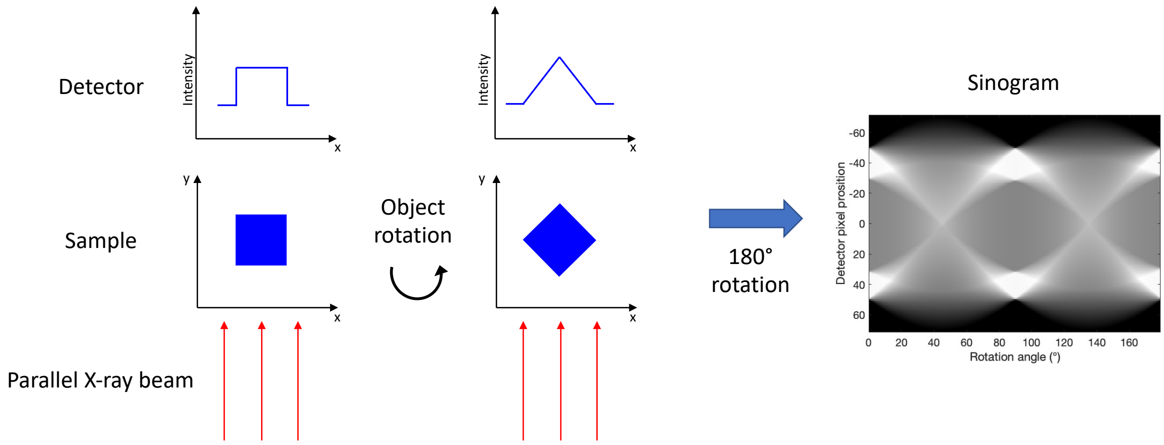

Figure 17. 2D illustration of an object absorbing X-rays and its projection on the detector at two different rotation angles. The sinogram is the combination of all rotations for one row of the detector.

A simplified example of a tomography experiment on a single-phase object and the projection on the detector is illustrated in **Figure 17**. The intensity profile is different depending on the angle of rotation and each angular step will give a projection on the detector. The compilation of these projections for one row of the detector is called the sinogram. To get the original object from the sinogram, a reconstruction algorithm needs to be used. This reconstruction algorithm is based on the Fourier slice theorem and is divided into 3 steps [54]:

- Take the Fourier transform of the projections.
- Apply a high pass filter.
- Use the Fourier slice theorem by taking the inverse of the 2D Fourier transform of the filtered set.

This algorithm, called Filtered Back-Projection (FBP), can reconstruct the original object based on the attenuation coefficient and is commonly used in XTM experiments. The filtering step is essential to alleviate artefacts due to the finite number of projections since the 2D Fourier space cannot be mapped completely and some data are missing at high frequencies, making simple back-projection often blurry compared to the original image, see **Figure 18**. Typically, a high-pass filter (such as the Ram-Lak filter) is applied to get a faithful reconstruction.

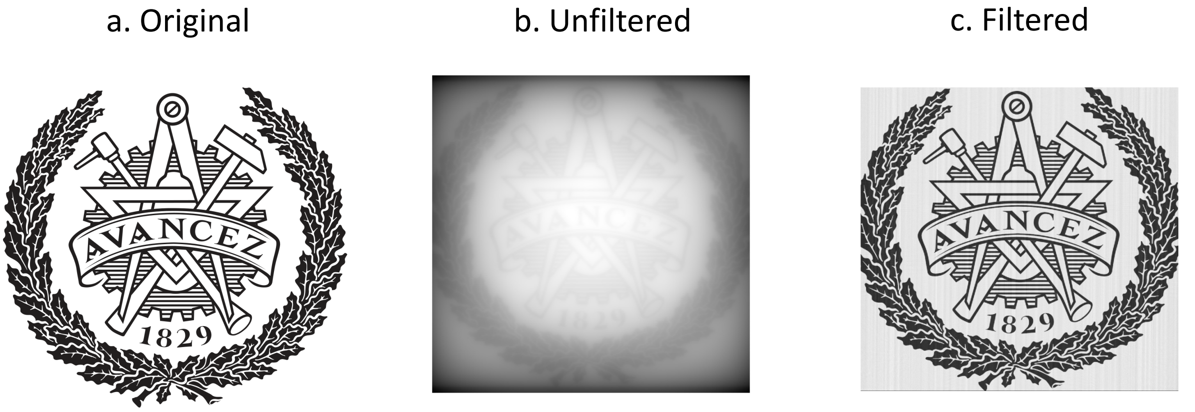
a. Original
b. Unfiltered
c. Filtered

Figure 18. a. original image of Chalmers logo, b. simple back projections reconstructed image and c. with the addition of the filtering step.

In addition to attenuation, the interaction of the X-ray with a material can induce a phase change of the transmitted beam compared to the incident beam. The phase change can help to distinguish different materials that have a weak absorption contrast from absorption-based tomography. A common route to also use phase contrast is the Paganin filter [83] which can be added to the reconstruction of the data.

There are also other important parameters to consider in a XTM experiment such as the field of view (FOV) and the pixel size. The camera detector is composed of a pixel array that has a certain size (e.g., a PCO Edge HS camera has 2560*2160 pixels of 6.5 µm each) and when combined with a magnification lens will give the voxel size and FOV (e.g., micrometre or nanometre). With the example of a PCO Edge camera detector combined with a x10 objective lens, the voxel size is thus 0.65 µm and FOV of 1664 µm in height and 1404 µm in width. However, with a x20 objective, the voxel size is 0.325 µm and the FOV is 832*702 μm^2. Lowering the voxel size to be able to resolve smaller objects with a larger magnification is done at the cost of a smaller FOV. A large FOV allows to capture the object of interest entirely and is crucial to carry out further quantitative analysis.

The resolution in the experiment is the size of the smallest object that can be distinguished in an image. With a 3D volume from a tomographic reconstruction, the resolution is about 3 times the size of a voxel since at least 3 voxels are needed to form an interface. As an example, the pixel size given by a detector was 0.332 µm at the ID19 beamline giving a resolution of approximately 1 µm. Practically, the determination of the actual spatial resolution can be done by plotting a line profile of the intensity along a sharp interface. **Figure 19** shows an interface between a porosity and a graphite particle where a line was drawn. The intensity profile of this line is plotted, and from this plot, it is possible to extract the image resolution. From **Figure 19**, the resolution is about 1.5 to 2 µm which is slightly higher than the estimation from the voxel size (1 µm).

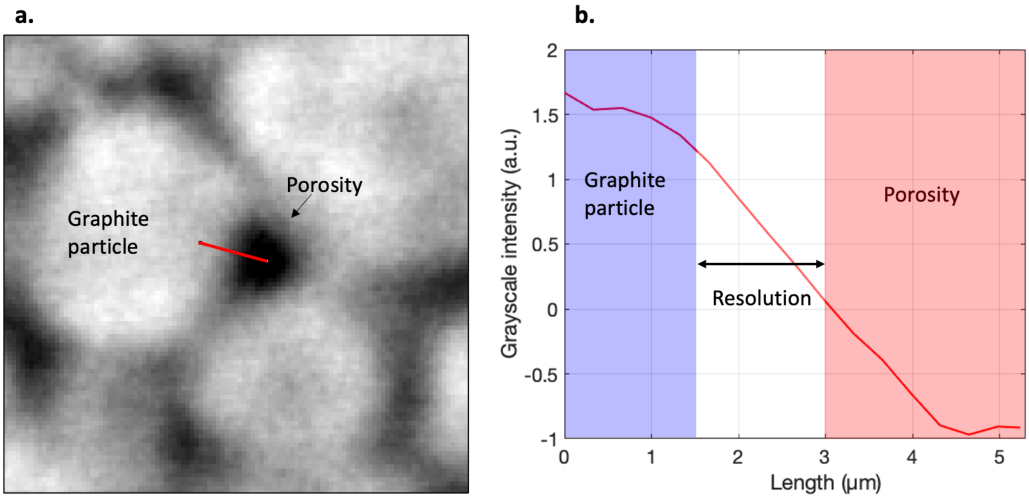

Figure 19. Determination of the resolution in a tomographic image. a. Zoomed tomographic 2D slice where a line is drawn at a sharp interface between a graphite particle (in bright colours) and a pore (dark). The resolution is given by the line intensity profile in b. at 10-90% of maximum and minimum intensities.

Getting quantitative data from XTM is often done by segmentation of the 3D data where the grayscale images produced by XTM have different values that can help separate the phases present. A simple approach to realise that is to set a threshold and create a binary image with the value 1 for every pixel above the threshold and 0 for the rest. That way, it is possible to quantify the number of voxels (and thus the volume when multiplied by the voxel size) of one phase.

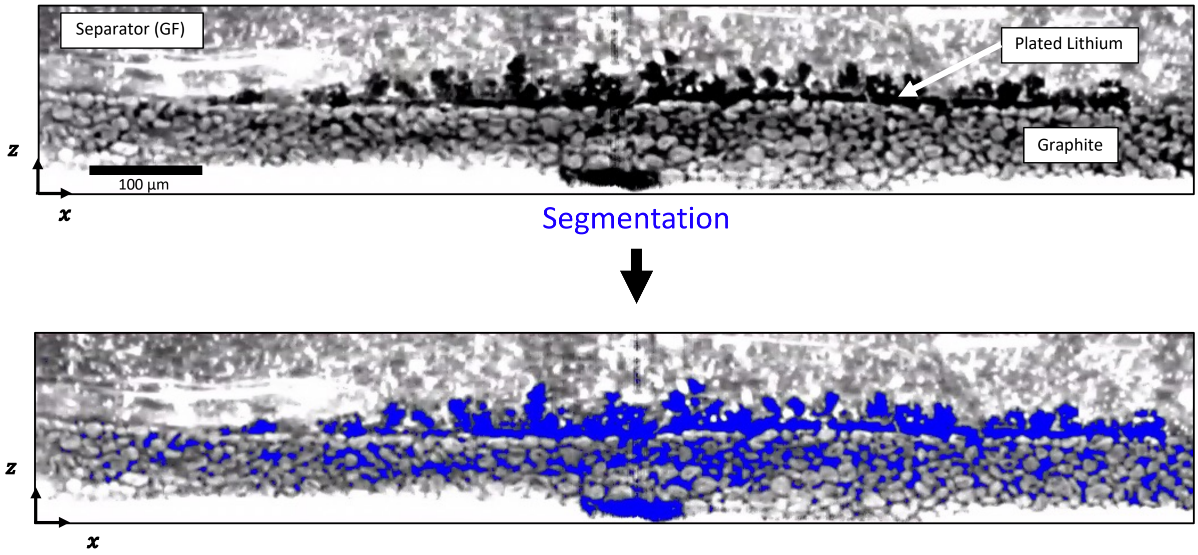

Figure 20. Example of segmentation of one tomographic slice with the different components of the cell (glass fibre separator and graphite anode). A blue overlay indicates the dark pixel that can be identified as plated Li.

Figure 20 shows a tomographic slice of a Li/graphite cell with a glass fibre separator and copper current collector. All the dark pixels in **Figure 20** are identified as one phase (plated lithium) and the other materials (graphite, copper, separator) are left out. From here, it is possible to quantify the amount of plated lithium. One issue with this simple segmentation approach is illustrated by this example since the pores filled with electrolyte are also identified as lithium. Further analysis must then be carried to only include relevant data from the tomographic slices, such as defining a region of interest (ROI), refining the threshold value, or changing the segmentation method (e.g., growing a mask from a seed, texture segmentation or watershed segmentation)

4 *Results & discussion*

This section discusses and puts into perspective the results from the attached papers (I-III). The overall scientific question addressed is: what are the morphological and structural changes in a battery electrode during charge and discharge? We observed the intercalation process followed by lithium plating in graphite, the pore-filling inhomogeneities of Na^+ in a hard carbon electrode, and the complex sulfur conversion in Li/S batteries.

4.1 Storage mechanism in carbonaceous materials

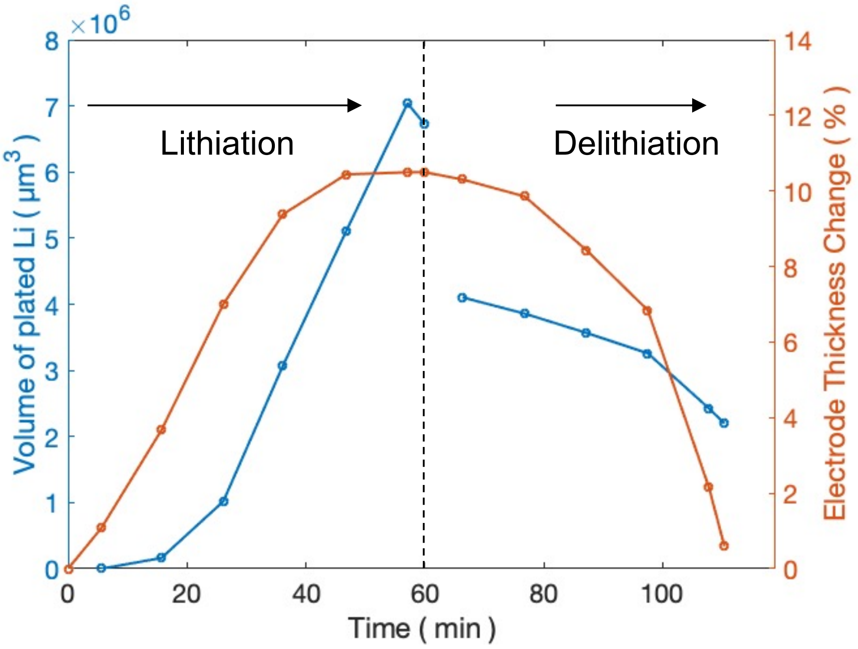

Figure 21. The volume of segmented plated lithium and electrode thickness change compared to the thickness of the pristine electrode.

Figure 21 shows data retrieved from XTM of a graphite/lithium PEEK cell. The electrode thickness change, compared to the pristine electrode and the segmented volume of plated Li is followed during lithiation and delithiation. The change in thickness of the electrode directly accounts for the state of lithiation of graphite since the intercalation of Li^+ between graphene layers increases their spacing, making the electrode swell by 10-13% (see section 2.2). The measurement of this change of thickness from the tomographic 2D slice enabled us to follow the lithiation and the subsequent delithiation of the graphite electrode by and isolating a region of interest and thresholding the plated lithium. From this analysis, it was possible to quantify the amount of plated Li and correlate the onset of the deposition with the state of charge and the voltage profile. By comparing the evolution of the two processes with the state of charge, we could conclude that the two processes occur sequentially during the lithiation, first the normal intercalation in graphite and then, the plating at the graphite/separator interface. Similarly, during delithiation, the plated lithium is partially stripped before Li ions are deintercalated from graphite, leaving dead lithium behind.

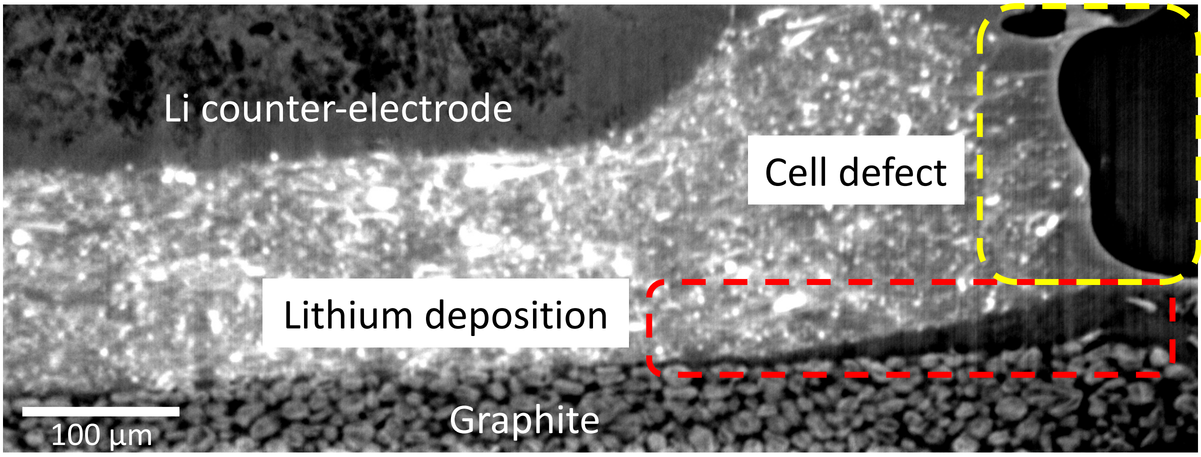

Figure 22. Tomogram cross section-slice highlighting the different features of the graphite-lithium cell and defect.

Figure 22 shows a 2D cross-section slice of a tomogram of a lithium-graphite stack in a PEEK cell. Graphite can be identified as grey particles and deposited lithium (framed in red) as black because of its low electron density. Lithium was deposited at the interface between the glass fibre separator and graphite. However, in this cell, we could observe a defect, framed in yellow, which could be a gas pocket or a space filled with electrolyte. We can see that the deposition seems to have occurred under this defect. It shows that the cell geometry and pressure distribution within the stack will affect, in this case, metal deposition. Moreover, the Li counter-electrode interface with the separator is not uniform, meaning that the lithium graphite distance is not constant, creating inhomogeneities in the cell. These two cell inhomogeneities show that defects caused by the cell assembly must be considered when analysing XTM data and there can be cell-to-cell variation.

The data from full-field XTM is a computed reconstruction of the electrode where each pixel has a grayscale value proportional to the electron density of a material. With a sufficiently low pixel size, it is possible to resolve lithium microstructures and graphite grains. In SAXS tomography, each pixel instead represents a scattering pattern which allows spatially resolve the state of charge of the electrode. This technique was performed at the cSAXS beamline at the Swiss Light Source of the Paul Scherrer Institute (Switzerland) on ex-situ hard carbon electrodes at different degrees of sodiation. Before the experiment, the cells were cycled in capillary cells then transferred to an empty capillary and sealed in a neutral atmosphere.

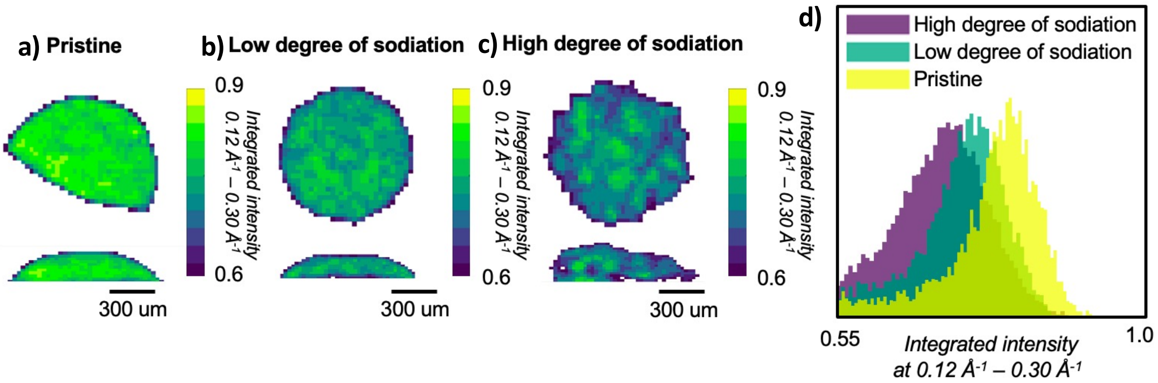

Figure 23. Integrated intensity of the microporous region of three samples at different degrees of sodiation from 2D slice of a computed tomographic volumes. a) a pristine hard carbon anode b) an anode with a low degree of sodiation and c) an anode with a high degree of sodiation. d) Histograms of the integrated intensity of the microporous q-regime for the three anodes.

The data presented in **Figure 23** are 2D slices where each pixel is an integrated value of the SAXS pattern in the q-range 0.12 Å – 0.3 Å which corresponds to the microporous regime (**Figure 14**). The scattering intensity in this regime is proportional to the difference in electron density of the carbon matrix and the micropores. The integrated intensity in this region is decreasing (**Figure 23d**) which indicates a micropore filling mechanism taking place during the sodiation of the electrode even at a low state of charge, in the slopping regime of the voltage profile. SAXS tomography can spatially resolve the electrode giving precise information on where the pore-filling mechanism is more advanced. The sodium-free electrode (**Figure 23a**) has homogenous micropore regime intensity but as the sodium concentration increases in the anode (**Figure 23b** & **c**), there is a spatial distribution of pore filling in the electrode. This shows that the filling of the micropores by Na$^+$ in a hard carbon electrode is not homogenous at high degrees of sodiation.

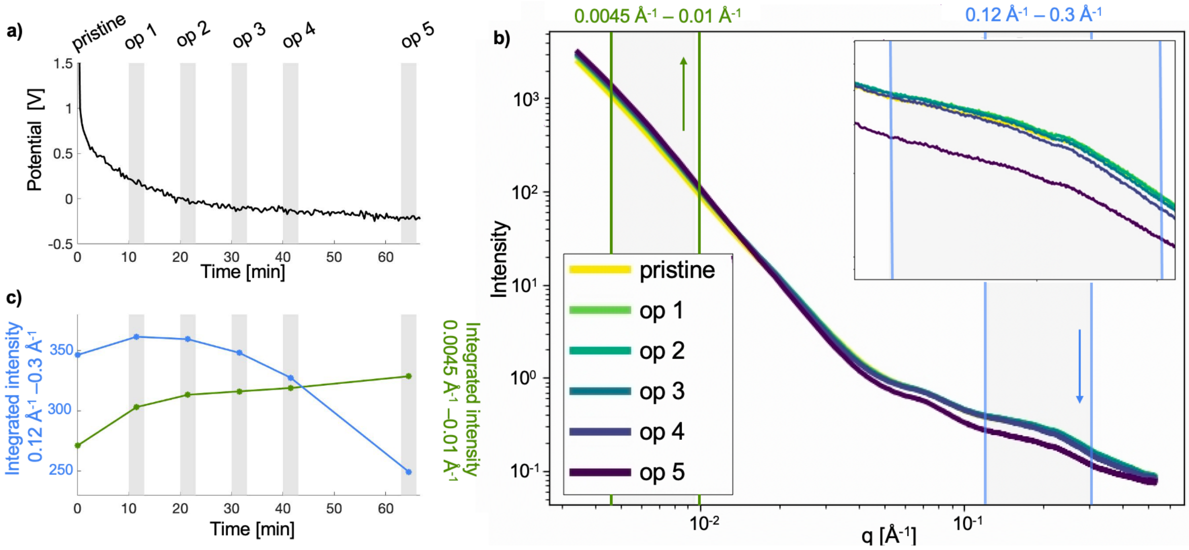

Figure 24. Results from *operando* measurements**.** a. Galvanostatic voltage profile of the sodiation of the hard carbon electrode. Grey lines indicate the points of collection of scanning S/WAXS images during the *operando* experiment (op #). b. Average SAXS curves of the anode at each time step. Inset shows a magnified view of the q-range corresponding to scattering from micropores. b. Integrated intensity in the q-regions corresponding to micropores (0.12-0.3 Å^{-1}) and hard carbon particle surface (0.0045-0.01 Å^{-1}) marked in b.

To obtain a deeper understanding of the sodiation process, a hard carbon-sodium cell was charged and the average SAXS pattern was obtained every 10 minutes, showing different features of sodiation in **Figure 24**. The quartz capillary cell used has much less background in the SAXS region compared to the scattering from PEEK. At the beginning of the charge, an increase in the integrated scattering intensity can be observed in the microporous region (0.12-0.3 Å^{-1}, **Figure 24b** & **c**). This can be interpreted as an increased contribution of the carbon matrix which implies that the intercalation of sodium in the hard carbon layers is the initial dominating process (in the slope region). Subsequently, the scattering intensity in the microporous region decreases suggesting a domination of a pore-filling mechanism in the plateau of the voltage profile (**Figure 24a**). The low q region (0.045-0.01 Å^{-1}) accounts for the hard carbon particle surface and roughness and cannot be directly correlated to sodiation. The phenomena that could be responsible for the continuous increased scattering intensity in this region are SEI formation, cracks and swelling of the grain surface. Since the increase in intensity is larger between the pristine and first scan, the formation of SEI could be a possible explanation.

From the result outlook of this section, one can observe the complementarity of S/WAXS tomography and full-field XTM. Both techniques can give qualitative and quantitative information through 3D modelling of an electrode. XTM is based on the different electron densities of materials in the cell and S/WAXS tomography on the elastic scattering of microstructures and both can resolve inhomogeneities and structural changes in a battery cell. However, it is worth noting that the time scales required for one scan in each technique are different. In XTM, depending on the desired resolution, the measurement time can vary between a few seconds and a few tens of minutes in modern synchrotron radiation facilities [84] (one minute for the graphite/lithium cell) whereas the acquisition time for SAXS tomography of the hard carbon anode was 7 hours long. It is of interest to perform both techniques sequentially where first XTM is used on the full electrode with fast scanning to identify regions of interest and then scan those regions with SAXS tomography. The combination of XTM and scattering techniques (S/WAXS) can be performed at different beamlines e.g., ForMAX at MAXIV (Lund, Sweden) or ID15a at ESRF (Grenoble, France).

4.2 Structural evolution of sulfur particles in Li/S batteries during cycling

This section is based on a continuation of the study of Sadd *et.al.* [57] where the dissolution of sulfur particles could be observed and quantified through *operando* XTM. Here we expanded the study by following both dissolution and precipitation of elemental sulfur in the composite electrode during charge and discharge. We carried out *operando* XTM at the ID15a beamline at ESRF (Grenoble, France) on a similar electrode composition but in a different cell compared to the previous work of Sadd *et.al.* [57] with the electrode cast on an aluminium foil and put into a PEEK cell with a glass fibre separator. This geometry did not allow for the full cathode in the field of view but, it is a more realistic configuration where also less electrolyte is used. After discharge and charge at different current densities (1C and 2C), tomographic scans were taken at the end of the charge and segmentation of the sulfur particles was performed.

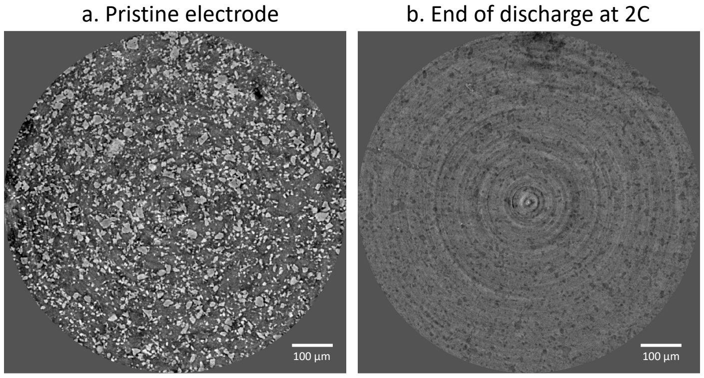
a. Pristine electrode

b. End of discharge at 2C

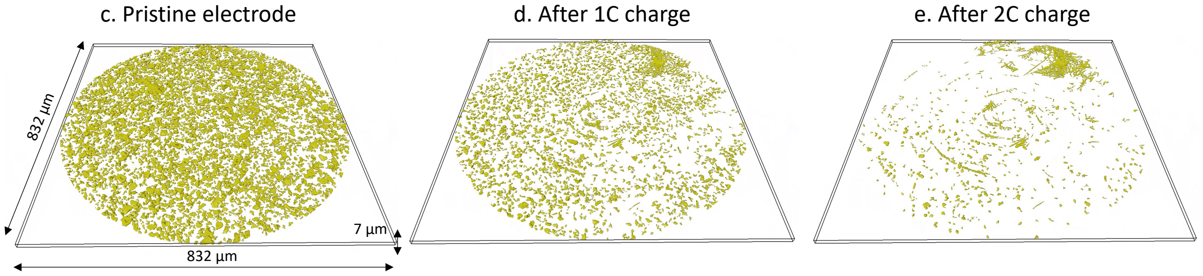
c. Pristine electrode

d. After 1C charge

e. After 2C charge

Figure 25. a, b Tomographic horizontal slices showing the pristine and the end of charge electrodes after 2C, respectively. c – e volume rendering of the cathode after charge with increasing current densities of the pristine electrode, after 1C charge, and after 2C charge respectively.

The complete dissolution of sulfur particles (**Figure 25a** & **b**) even after a discharge at a current rate of 2C could suggest that the conversion of elemental sulfur into long chain polysulfides is not rate-limiting. One can consider that at higher rates, polysulfides don’t have the time to diffuse out the carbon matrix which makes their subsequent redeposition more homogenous. Indeed. the 3D renderings of segmented sulfur particles after the charge (**Figure 25c-e**) show that elemental sulfur precipitates evenly in the cathode. However, it is clear that fewer elemental sulfur particles precipitate at the end of the charge and this effect is enhanced by increasing current density and could explain poor cyclability. To quantify changes in particle size, the particle size distribution has been extracted from segmented data and is shown in **Figure 26**.

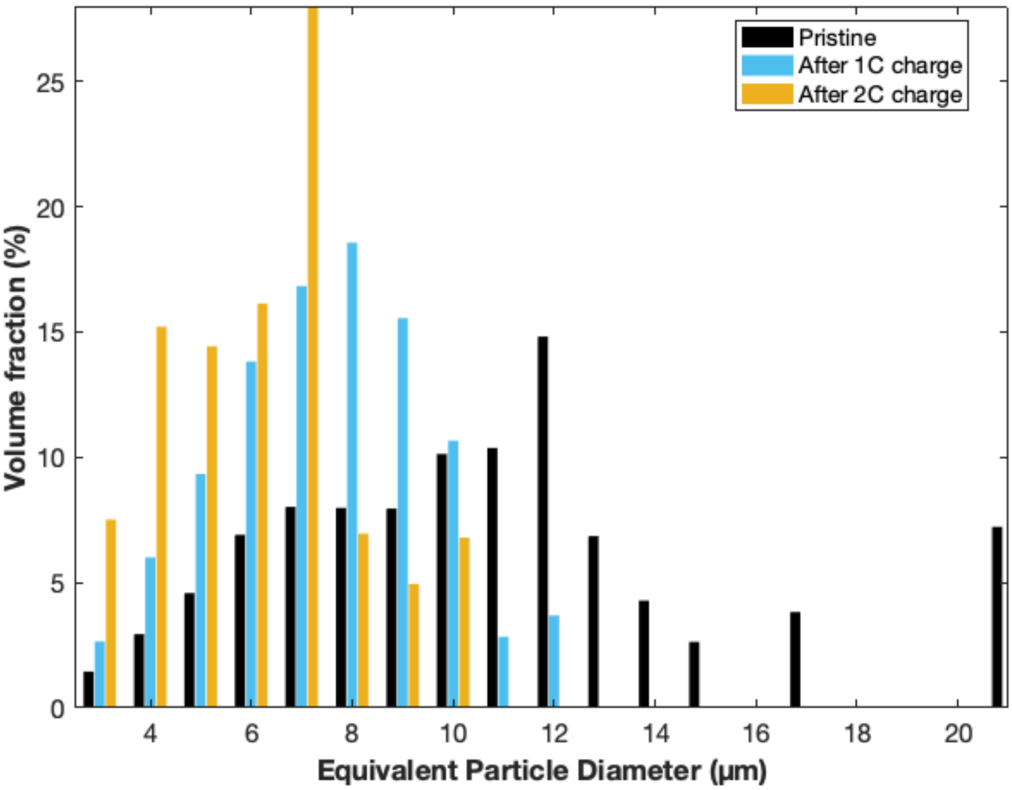

Figure 26. Distribution of the percentage of sulfur particles as a function of particle size of an equivalent spherical diameter in the pristine cathode and after charge at 1C and 2C

The volume of a sphere of an equivalent diameter was plotted to better visualise the distribution of particle size. Additionally, the distribution was scaled to the total volume of segmented sulfur to better represent the larger particles since their frequency is lower compared to the small particles (diameter < 4 µm). Small particles represent a fraction < 5 % of the total sulfur volume so their contribution to the electrode capacity can in principle be neglected. The isolated bar at 21 µm in the pristine volume is likely to be an error in the segmentation where a larger particle was not well separated by a watershed. From **Figure 26**, we observe a decrease in the average size of the particles after cycling. The effect is larger with a larger current density. This can be associated with the formation of smaller nuclei that precipitate in new particles rather than the growth from an existing nucleation site. An improvement to these data could be to segment the full electrode within the field of view and not only a cropped volume. However, this represents a challenge with simple thresholding since the grayscale intensity of the separator's fibre is very close to the one of the sulfur.

5 Conclusion & Outlook

In this thesis, X-ray imaging has been used to track morphological changes in battery electrodes through *operando* measurement, with high temporal and/or spatial resolution. The complex chemistry and large variety of battery systems require advanced characterisation methods to reach the deepest understanding possible of the processes. Here, three very different types of storage mechanisms are investigated. We show that fast data acquisition in synchrotron-based tomography enables us to track the different processes taking place in a graphite electrode, from the classic intercalation of lithium ions to the normally unwanted metallic deposition. SAXS tomography allowed us to follow changes in the microporous regime of a hard carbon electrode as an indicator of the sodiation state with the correlation of electrochemical data. We show that the pore-filling mechanism responsible for the energy storage is not spatially homogenous in the electrode and the degree of inhomogeneities increases with the state of charge. XTM enabled the direct observation of a sulfur composite electrode, giving detailed insights into the dissolution and precipitation of elemental sulfur. Through the analysis of the size distribution of sulfur particles, we showed a decreased overall particle diameter compared to the uncycled electrode after the charge. The complete dissolution of elemental sulfur even at high current densities indicates that the conversion reaction into long-chain polysulfides is not rate-limited.

There are multiple paths to explore to improve the comprehension we have of the battery chemistries studied here. First, to localise the inhomogeneities of lithium intercalation in graphite, it is possible to perform Digital Volume Correlation (DVC) since it keeps track of displacement fields in a structure, which can be linked to the graphite lithiation. Additionally, the low contrast in tomography data between plated Li and pores between graphite particles makes them challenging to differentiate. We plan to carry out *operando* S/WAXS tomography to identify the onset of plating in the bulk of the electrode. This will be combined with XTM at the ForMAX beamline. Moving to XTM performed on a Li/S cell, the full electrode within the FOV should be considered when performing a quantitative analysis. This can be done by advanced segmentation methods such as gradient segmentation. Finally, more complementary work will be carried out for decoupling the contribution of the electrolyte in the pore-filling mechanism of hard carbons to identify SAXS features from ex-situ and *operando* data.

Acknowledgements

First and foremost, I would like to thank the Swedish Energy Agency for founding my position, CIDITEC and the Big-Map project for providing the necessary materials for the projects.

Then, I want to give a massive thanks to my PhD advisor Aleksandar Matic. I truly do not understand how you can keep being so enthusiastic despite all the troubles I am giving you. Thank you for all the time you dedicated to great discussion and scientific advice with me. I can grow as a better researcher and person thanks to you.

A big thanks to my examiner, Patrik Johansson, your scientific knowledge of batteries enabled me to understand my topic better. A special thanks to my assistant supervisor, Shizhao Xiong for the countless times I popped into your office with many questions, you have always been there for guidance when I needed it.

Then, I would like to warmly thank all the members of the Material Physics division. The spirit in the lab is just so great and it is not something I have experienced in many workplaces. Among them, a special thanks to Martina Olsson, my beamtime partner, who did all the data analysis and writing in Paper III, you provided fantastic effort and help.

A big thanks to Matthew Sadd who not only helped me a lot in moving to Sweden but also in the lab by sharing with me all the tips and tricks he acquired during his PhD journey. This work wouldn’t have existed without you.

I also want to thank Nataliia Mozhzhukhina for being such a great office mate. I came to you with so many questions (battery-related or not) and you could always help me with your answers.

Finally, I want to give a special thanks to my friends and family in France, for all your support.

References

[1] R. Palacin, 'Recent advances in rechargeable battery materials: a chemist's perspective', *Chemical Society Reviews*, vol: 38, no. 9, pp. 2565-2575, 2009, doi: 10.1039/b820555h.

[2] M. Armand and J. M. Tarascon, 'Building better batteries', *Nature*, vol. 451, no. 7179, pp. 652–657, Feb. 2008, doi: 10.1038/451652A.

[3] 'Delivering the European Green Deal'. Accessed: Nov. 16, 2023. [Online]. Available: https://commission.europa.eu/strategy-and-policy/priorities-2019-2024/european-green-deal/delivering-european-green-deal_en

[4] C. Delmas, 'Sodium and Sodium-Ion Batteries: 50 Years of Research', *Advanced Energy Materials*, vol. 8, no. 17, p. 1703137, 2018, doi: 10.1002/aenm.201703137.

[5] X. Ji and L. F. Nazar, 'Advances in Li–S batteries', *J. Mater. Chem.*, vol. 20, no. 44, pp. 9821–9826, Nov. 2010, doi: 10.1039/B925751A.

[6] Z. Rogulski and A. Czerwiński, 'Cathode modification in the Leclanché cell', *J Solid State Electrochem*, vol. 7, no. 2, pp. 118–121, Feb. 2003, doi: 10.1007/s10008-002-0322-3.

[7] H. F. McMurdie, D. N. Craig, and G. W. Vinal, 'A Study of Equilibrium Reactions in the Leclanché Dry Cell', *Trans. Electrochem. Soc.*, vol. 90, no. 1, p. 509, 1946, doi: 10.1149/1.3071763.

[8] A. Yoshino, 'The Birth of the Lithium-Ion Battery', *Angewandte Chemie International Edition*, vol. 51, no. 24, pp. 5798–5800, 2012, doi: 10.1002/anie.201105006.

[9] M. S. Whittingham, 'Electrical Energy Storage and Intercalation Chemistry', *Science*, vol. 192, no. 4244, pp. 1126-1127, 1976, doi: 10.1126/science.192.4244.1126.

[10] J. B. Goodenough. K.Mizushima, P.C.Jones, P.J.Wiseman, 'LixCoO2 (0<x<-1): A new cathode material for batteries of high energy density', *Mater. Res. Bull. 1980*, vol. 42, no. 9 B, pp. 6131–6134, 1979, doi: https://doi.org/10.1016/0025-5408(80)90012-4.

[11] R. Yazami and P. Touzain, 'A reversible graphite-lithium negative electrode for electrochemical generators', *Journal of Power Sources*, vol. 9, no. 3, pp. 365–371, 1983, doi: 10.1016/0378-7753(83)87040-2.

[12] 'The Nobel Prize in chemistry 2019'. Accessed: Nov. 16, 2023. [Online]. Available: https://www.nobelprize.org/prizes/chemistry/2019/press-release/

[13] J. Xu *et al.*, 'High-Energy Lithium-Ion Batteries: Recent Progress and a Promising Future in Applications', *ENERGY & ENVIRONMENTAL MATERIALS*, vol. 6, no. 5, p. e12450, 2023, doi: 10.1002/eem2.12450.

[14] D. Allart, M. Montaru, and H. Gualous, 'Model of Lithium Intercalation into Graphite by Potentiometric Analysis with Equilibrium and Entropy Change Curves of Graphite Electrode', *J. Electrochem. Soc.*, vol. 165, no. 2, p. A380, Feb. 2018, doi: 10.1149/2.1251802jes.

[15] M. R. Palacín and A. de Guibert, 'Why do batteries fail?', *Science*, vol. 351, no. 6273, p. 1253292, Feb. 2016, doi: 10.1126/science.1253292.

[16] E. Peled, 'The Electrochemical Behavior of Alkali and Alkaline Earth Metals in Nonaqueous Battery Systems—The Solid Electrolyte Interphase Model', *J. Electrochem. Soc.*, vol. 126, no. 12, pp. 2047–2051, Dec. 1979, doi: 10.1149/1.2128859.

[17] H. Wu, H. Jia, C. Wang, J.-G. Zhang, and W. Xu, 'Recent Progress in Understanding Solid Electrolyte Interphase on Lithium Metal Anodes', *Advanced Energy Materials*, vol. 11, no. 5, p. 2003092, 2021, doi: 10.1002/aenm.202003092.

[18] E. Peled and S. Menkin, 'Review—SEI: Past, Present and Future', *Journal of The Electrochemical Society*, vol. 164, no. 7, pp. A1703–A1719, Jun. 2017, doi: 10.1149/2.1441707jes.

[19] J. Asenbauer, T. Eisenmann, M. Kuenzel, A. Kazzazi, Z. Chen, and D. Bresser, 'The success story of graphite as a lithium-ion anode material – fundamentals, remaining challenges, and recent developments including silicon (oxide) composites', *Sustainable Energy & Fuels*, vol. 4, no. 11, pp. 5387–5416, Oct. 2020, doi: 10.1039/D0SE00175A.

[20] S. Schweidler, L. De Biasi, A. Schiele, P. Hartmann, T. Brezesinski, and J. Janek, 'Volume Changes of Graphite Anodes Revisited: A Combined Operando X-ray Diffraction and in Situ Pressure Analysis Study', *Journal of Physical Chemistry C*, vol. 122, no. 16, pp. 8829–8835, Apr. 2018, doi: 10.1021/acs.jpcc.8b01873.

[21] M. Winter, J. O. Besenhard, M. E. Spahr, and P. Novák, ‘Insertion Electrode Materials for Rechargeable Lithium Batteries’, *Advanced Materials*, vol. 10, no. 10, pp. 725–763, 1998, doi: 10.1002/(SICI)1521-4095(199807)10:10<725::AID-ADMA725>3.0.CO;2-Z

[22] A. S. Ho *et al.*, ‘3D Detection of Lithiation and Lithium Plating in Graphite Anodes during Fast Charging’, *ACS Nano,* vol. 15, no. 6, pp. 10480-10487, 2021, doi: 10.1021/acsnano.1c02942.

[23] J. R. Dahn, R. F. Moli, and M. J. Spoon, ‘Suppression of staging in lithium-intercalated carbon by disorder in the host’, *PHYSICAL REVIEW B*, vol. 42, no. 10, p. 6424, 1990, doi: https://doi.org/10.1103/PhysRevB.42.6424.

[24] M. N. Obrovac and V. L. Chevrier, ‘Alloy negative electrodes for Li-ion batteries’, *Chemical Reviews*, vol. 114, no. 23, pp. 11444–11502, 2014, doi: 10.1021/cr500207g.

[25] D. Hu *et al.*, ‘Research Progress of Lithium Plating on Graphite Anode in Lithium-Ion Batteries’, *Chinese Journal of Chemistry*, vol. 39, no. 1, pp. 165–173, 2021, doi: 10.1002/cjoc.202000512.

[26] M. Petzl and M. A. Danzer, ‘Nondestructive detection, characterization, and quantification of lithium plating in commercial lithium-ion batteries’, *Journal of Power Sources*, vol. 254, pp. 80–87, May 2014, doi: 10.1016/j.jpowsour.2013.12.060.

[27] X. Lin, K. Khosravinia, X. Hu, J. Li, and W. Lu, ‘Lithium Plating Mechanism, Detection, and Mitigation in Lithium-Ion Batteries’, *Progress in Energy and Combustion Science*, vol. 87, p. 100953, Nov. 2021, doi: 10.1016/J.PECS.2021.100953.

[28] Y. Ji, Y. Zhang, and C.-Y. Wang, ‘Li-Ion Cell Operation at Low Temperatures’, *J. Electrochem. Soc.*, vol. 160, no. 4, p. A636, Feb. 2013, doi: 10.1149/2.047304jes.

[29] X. Zhao, Y. Yin, Y. Hu, and S.-Y. Choe, ‘Electrochemical-thermal modeling of lithium plating/stripping of Li(Ni0.6Mn0.2Co0.2)O2/Carbon lithium-ion batteries at subzero ambient temperatures’, *Journal of Power Sources*, vol. 418, pp. 61–73, Apr. 2019, doi: 10.1016/j.jpowsour.2019.02.001.

[30] K. N. Wood *et al.*, ‘Dendrites and Pits: Untangling the Complex Behavior of Lithium Metal Anodes through Operando Video Microscopy’, *ACS Central Science*, vol. 2, no. 11, pp. 790–801, Nov. 2016, doi: 10.1021/acscentsci.6b00260.

[31] Y. Li, X. Feng, D. Ren, M. Ouyang, L. Lu, and X. Han, ‘Thermal Runaway Triggered by Plated Lithium on the Anode after Fast Charging’, *ACS Appl. Mater. Interfaces*, vol. 11, no. 50, pp. 46839–46850, Dec. 2019, doi: 10.1021/acsami.9b16589.

[32] Q. Liu *et al.*, ‘Understanding undesirable anode lithium plating issues in lithium-ion batteries’, *RSC Advances,* vol. 6, no. 91, pp. 88683-88700, 2016, doi: 10.1039/c6ra19482f.

[33] C. R. Birkl, M. R. Roberts, E. McTurk, P. G. Bruce, and D. A. Howey, ‘Degradation diagnostics for lithium ion cells’, *Journal of Power Sources*, vol. 341, pp. 373–386, Feb. 2017, doi: 10.1016/j.jpowsour.2016.12.011.

[34] J. P. Jones, M. C. Smart, F. C Krause and R. V. Bugga ‘The Effect of Electrolyte Additives upon Lithium Plating during Low Temperature Charging of Graphite-LiNiCoAlO 2 Lithium-Ion Three Electrode Cells’, vol. 167, no. 2, pp. 020536, 2020, doi: 10.1149/1945-7111/ab6bc2.

[35] J. C. Burns *et al.*, ‘Studies of the Effect of Varying Vinylene Carbonate (VC) Content in Lithium Ion Cells on Cycling Performance and Cell Impedance’, *Journal of The Electrochemical Society*, vol. 160, no. 10, pp. A1668–A1674, 2013, doi: 10.1149/2.031310jes.

[36] M. C. Smart, B. L. Lucht, S. Dalavi, F. C. Krause, and B. V. Ratnakumar, ‘The Effect of Additives upon the Performance of MCMB/LiNixCo1−xO2 Li-Ion Cells Containing Methyl Butyrate-Based Wide Operating Temperature Range Electrolytes’, *J. Electrochem. Soc.*, vol. 159, no. 6, p. A739, Apr. 2012, doi: 10.1149/2.058206jes.

[37] V. Sharova, A. Moretti, T. Diemant, A. Varzi, R. J. Behm, and S. Passerini, ‘Comparative study of imide-based Li salts as electrolyte additives for Li-ion batteries’, *Journal of Power Sources*, vol. 375, pp. 43–52, Jan. 2018, doi: 10.1016/j.jpowsour.2017.11.045.

[38] X. Peng, Y. Lin, Y. Wang, Y. Li, and T. Zhao, ‘A lightweight localized high-concentration ether electrolyte for high-voltage Li-Ion and Li-metal batteries’, *Nano Energy*, vol. 96, p. 107102, Jun. 2022, doi: 10.1016/j.nanoen.2022.107102.

[39] L. Somerville, S. Ferrari, M. J. Lain, A. McGordon, P. Jennings, and R. Bhagat, ‘An In-Situ Reference Electrode Insertion Method for Commercial 18650-Type Cells’, *Batteries*, vol. 4, no. 2, Art. no. 2, Jun. 2018, doi: 10.3390/batteries4020018.

[40] E. McTurk, C. R. Birkl, M. R. Roberts, D. A. Howey, and P. G. Bruce, ‘Minimally Invasive Insertion of Reference Electrodes into Commercial Lithium-Ion Pouch Cells’, *ECS Electrochem. Lett.*, vol. 4, no. 12, p. A145, Jan. 2015, doi: 10.1149/2.0081512eel.

[41] M. Dubarry, V. Svoboda, R. Hwu, and B. Yann Liaw, ‘Incremental Capacity Analysis and Close-to-Equilibrium OCV Measurements to Quantify Capacity Fade in Commercial Rechargeable Lithium Batteries’, *Electrochem. Solid-State Lett.*, vol. 9, no. 10, p. A454, 2006, doi: 10.1149/1.2221767.

[42] I. D. Campbell, M. Marzook, M. Marinescu, and G. J. Offer, ‘How Observable Is Lithium Plating? Differential Voltage Analysis to Identify and Quantify Lithium Plating Following Fast Charging of Cold Lithium-Ion Batteries’, *Journal of The Electrochemical Society*, vol. 166, no. 4, pp. A725–A739, 2019, doi: 10.1149/2.0821904jes.

[43] C. Martin, M. Genovese, A. J. Louli, R. Weber, and J. R. Dahn, ‘Cycling Lithium Metal on Graphite to Form Hybrid Lithium-Ion/Lithium Metal Cells’, *Joule*, vol. 4, no. 6, pp. 1296–1310, Jun. 2020, doi: 10.1016/j.joule.2020.04.003.

[44] R. Mogi, M. Inaba, Y. Iriyama, T. Abe, and Z. Ogumi, ‘In Situ Atomic Force Microscopy Study on Lithium Deposition on Nickel Substrates at Elevated Temperatures’, *J. Electrochem. Soc.*, vol. 149, no. 4, p. A385, Feb. 2002, doi: 10.1149/1.1454138.

[45] R. L. Sacci *et al.*, ‘Direct visualization of initial SEI morphology and growth kinetics during lithium deposition by in situ electrochemical transmission electron microscopy’, *Chem. Commun.*, vol. 50, no. 17, pp. 2104–2107, Jan. 2014, doi: 10.1039/C3CC49029G.

[46] T. Gao *et al.*, ‘Interplay of Lithium Intercalation and Plating on a Single Graphite Particle’, *Joule*, vol. 5, no. 2, pp. 393–414, 2021, doi: 10.1016/j.joule.2020.12.020.

[47] R. Bhattacharyya, B. Key, H. Chen, A. S. Best, A. F. Hollenkamp, and C. P. Grey, ‘In situ NMR observation of the formation of metallic lithium microstructures in lithium batteries’, *Nature Mater*, vol. 9, no. 6, Art. no. 6, Jun. 2010, doi: 10.1038/nmat2764.

[48] H. J. Chang *et al.*, ‘Investigating Li Microstructure Formation on Li Anodes for Lithium Batteries by in Situ 6Li/7Li NMR and SEM’, *J. Phys. Chem. C*, vol. 119, no. 29, pp. 16443–16451, Jul. 2015, doi: 10.1021/acs.jpcc.5b03396.

[49] M. T. Fonseca Rodrigues *et al.*, ‘Lithium acetylide: A spectroscopic marker for lithium deposition during fast charging of Li-ion cells’, *ACS Applied Energy Materials*, vol. 2, no. 1, pp. 873–881, Jan. 2019, doi: https://doi.org/10.1021/acsaem.8b01975.

[50] M. A. Cabañero, M. Hagen, and E. Quiroga-González, ‘In-operando Raman study of lithium plating on graphite electrodes of lithium ion batteries’, *Electrochimica Acta*, vol. 374, p. 137487, Apr. 2021, doi: 10.1016/J.ELECTACTA.2020.137487.

[51] M. Sadd, S. Xiong, J. R. Bowen, F. Marone, and A. Matic, ‘Investigating microstructure evolution of lithium metal during plating and stripping via operando X-ray tomographic microscopy’, *Nature Communications*, vol. 14, no. 1, p.854 2023, doi: 10.1038/s41467-023-36568-z.

[52] K. Dong *et al.*, ‘Non-destructive characterization of lithium deposition at the Li/separator and Li/carbon matrix interregion by synchrotron X-ray tomography’, *Nano Energy*, vol. 62, no. May, pp. 11–19, 2019, doi: 10.1016/j.nanoen.2019.05.022.

[53] M. Yusuf *et al.*, ‘Simultaneous neutron and X-ray tomography for visualization of graphite electrode degradation in fast-charged lithium-ion batteries’, *Cell Reports Physical Science*, p. 101145, 2022, doi: 10.1016/j.xcrp.2022.101145.

[54] P. Pietsch and V. Wood, ‘X-Ray Tomography for Lithium Ion Battery Research: A Practical Guide’, *Annual Review of Materials Research*, vol. 47, pp. 451–479, 2017, doi: 10.1146/annurev-matsci-070616-123957.

[55] R. Fang, S. Zhao, Z. Sun, D.-W. Wang, H.-M. Cheng, and F. Li, ‘More Reliable Lithium-Sulfur Batteries: Status, Solutions and Prospects’, *Advanced Materials*, vol. 29, no. 48, p. 1606823, 2017, doi: 10.1002/adma.201606823.

[56] A. Manthiram, Y. Fu, S.-H. Chung, C. Zu, and Y.-S. Su, ‘Rechargeable Lithium–Sulfur Batteries’, *Chem. Rev.*, vol. 114, no. 23, pp. 11751–11787, Dec. 2014, doi: 10.1021/cr500062v.

[57] M. Sadd *et al.*, ‘Visualization of Dissolution-Precipitation Processes in Lithium–Sulfur Batteries’, *Advanced Energy Materials*, vol. 12, no. 10, p. 2103126, Jan. 2022, doi: 10.1002/AENM.202103126.

[58]J. Conder, R. Bouchet, S. Trabesinger, C. Marino, L. Gubler, and C. Villevieille, ‘Direct observation of lithium polysulfides in lithium-sulfur batteries using operando X-ray diffraction’, *Nature Energy*, vol. 2, no. May, pp. 1–7, 2017, doi: 10.1038/nenergy.2017.69.

[59]X. Li, L. Yuan, D. Liu, J. Xiang, Z. Li, and Y. Huang, ‘Solid/Quasi-Solid Phase Conversion of Sulfur in Lithium–Sulfur Battery’, *Small*, vol. 18, no. 43, pp. 1–29, 2022, doi: 10.1002/smll.202106970.

[60]J. Conder, C. Villevieille, S. Trabesinger, P. Novák, L. Gubler, and R. Bouchet, ‘Electrochemical impedance spectroscopy of a Li–S battery: Part 1. Influence of the electrode and electrolyte compositions on the impedance of symmetric cells’, *Electrochimica Acta*, vol. 244, pp. 61–68, Aug. 2017, doi: 10.1016/j.electacta.2017.05.041.

[61]Y. Diao, K. Xie, S. Xiong, and X. Hong, ‘Shuttle phenomenon e The irreversible oxidation mechanism of sulfur active material in Li e S battery’, *Journal of Power Sources*, vol. 235, pp. 181–186, 2013, doi: 10.1016/j.jpowsour.2013.01.132.

[62]M. Agostini, S. Xiong, A. Matic, and J. Hassoun, ‘Polysulfide-containing Glyme-based Electrolytes for Lithium Sulfur Battery’, *Chemistry of Materials*, vol. 27, no. 13, pp. 4604–4611, Jul. 2015, doi: 10.1021/acs.chemmater.5b00896.

[63]Y. Liu *et al.*, ‘Electrolyte solutions design for lithium-sulfur batteries’, *Joule*, vol. 5, no. 9, pp. 2323–2364, Sep. 2021, doi: 10.1016/j.joule.2021.06.009.

[64]Q. Pang, A. Shyamsunder, B. Narayanan, C. Y. Kwok, L. A. Curtiss, and L. F. Nazar, ‘Tuning the electrolyte network structure to invoke quasi-solid state sulfur conversion and suppress lithium dendrite formation in Li–S batteries’, *Nature Energy*, vol. 3, no. 9, pp. 783–791, 2018, doi: 10.1038/s41560-018-0214-0.

[65]J. Castillo *et al.*, ‘Graphene-Based Sulfur Cathodes and Dual Salt-Based Sparingly Solvating Electrolytes: A Perfect Marriage for High Performing, Safe, and Long Cycle Life Lithium-Sulfur Prototype Batteries’, *Advanced Energy Materials*, vol. 14, no. 1, p. 2302378, Nov. 2023, doi: 10.1002/aenm.202302378.

[66]R. Bouchal, A. Boulaoued, and P. Johansson, ‘Monitoring Polysulfide Solubility and Diffusion in Fluorinated Ether-Based Electrolytes by Operando Raman Spectroscopy’, *Batteries & Supercaps*, vol. 3, no. 5, pp. 397–401, 2020, doi: 10.1002/batt.201900188.

[67]A. Yermukhambetova *et al.*, ‘Exploring 3D microstructural evolution in Li-Sulfur battery electrodes using in-situ X-ray tomography’, *Scientific Reports 2016 6:1*, vol. 6, no. 1, pp. 1–9, Oct. 2016, doi: 10.1038/srep35291.

[68]C. Tan *et al.*, ‘Four-Dimensional Studies of Morphology Evolution in Lithium–Sulfur Batteries’, *ACS Appl. Energy Mater.*, vol. 1, no. 9, pp. 5090–5100, Sep. 2018, doi: 10.1021/acsaem.8b01148.

[69]L. Zielke *et al.*, ‘Degradation of Li/S Battery Electrodes On 3D Current Collectors Studied Using X-ray Phase Contrast Tomography’, *Sci Rep*, vol. 5, no. 1, no. 1, Jun. 2015, doi: 10.1038/srep10921.

[70]M. D. Slater, D. Kim, E. Lee, and C. S. Johnson, ‘Sodium-Ion Batteries’, *Advanced Functional Materials*, vol. 23, no. 8, pp. 947–958, 2013, doi: 10.1002/adfm.201200691.

[71]D. Saurel *et al.*, ‘A SAXS outlook on disordered carbonaceous materials for electrochemical energy storage’, *Energy Storage Materials*, vol. 21, pp. 162–173, 2019, doi: 10.1016/j.ensm.2019.05.007.

[72]X. Chen, Y. Zheng, W. Liu, C. Zhang, S. Li, and J. Li, ‘High-performance sodium-ion batteries with a hard carbon anode: transition from the half-cell to full-cell perspective’, *Nanoscale*, vol. 11, no. 46, pp. 22196–22205, Nov. 2019, doi: 10.1039/C9NR07545C.

[73]C. Zhao, Q. Wang, Y. Lu, B. Li, L. Chen, and Y.-S. Hu, ‘High-temperature treatment induced carbon anode with ultrahigh Na storage capacity at low-voltage plateau’, *Science Bulletin*, vol. 63, no. 17, pp. 1125–1129, Sep. 2018, doi: 10.1016/j.scib.2018.07.018.

[74]L. Kitsu Iglesias *et al.*, ‘Revealing the Sodium Storage Mechanisms in Hard Carbon Pores’, *Advanced Energy Materials*, vol. 13 no. 44, p. 2302171, 2023, doi: 10.1002/aenm.202302171.

[75]Y. Morikawa, S. Nishimura, R. Hashimoto, M. Ohnuma, and A. Yamada, ‘Mechanism of Sodium Storage in Hard Carbon: An X-Ray Scattering Analysis’, *Advanced Energy Materials*, vol. 10, no. 3, p. 1903176, 2020, doi: 10.1002/aenm.201903176.

[76]D. A. Stevens and J. R. Dahn, ‘An In Situ Small-Angle X-Ray Scattering Study of Sodium Insertion into a Nanoporous Carbon Anode Material within an Operating Electrochemical Cell’, *J. Electrochem. Soc.*, vol. 147, no. 12, p. 4428, Dec. 2000, doi: 10.1149/1.1394081.

[77] D. P. Finegan *et al.*, ‘Spatial dynamics of lithiation and lithium plating during high-rate operation of graphite electrodes’, *Energy & Environmental Science*, vol. 13, no. 8, pp. 2570–2584, Aug. 2020, doi: 10.1039/D0EE01191F.

[78] S. J. Talley, S. L. Vivod, B. A. Nguyen, M. A. B. Meador, A. Radulescu, and R. B. Moore, ‘Hierarchical Morphology of Poly(ether ether ketone) Aerogels’, *ACS Appl. Mater. Interfaces*, vol. 11, no. 34, pp. 31508–31519, Aug. 2019, doi: 10.1021/acsami.9b09699.

[79] F. Schaff *et al.*, ‘Six-dimensional real and reciprocal space small-angle X-ray scattering tomography’, *Nature*, vol. 527, no. 7578, no. 7578, Nov. 2015, doi: 10.1038/nature16060.

[80] D. P. Finegan *et al.*, ‘In-operando high-speed tomography of lithium-ion batteries during thermal runaway’, *Nat Commun*, vol. 6, no. 1, no. 1, Apr. 2015, doi: 10.1038/ncomms7924.

[81] J. Li *et al.*, ‘Dynamics of particle network in composite battery cathodes’, *Science*, vol. 376, no. 6592, pp. 517–521, Apr. 2022, doi: 10.1126/SCIENCE.ABM8962.

[82] B. L. Henke, E. M. Gullikson, and J. C. Davis, ‘X-Ray Interactions: Photoabsorption, Scattering, Transmission, and Reflection at E = 50-30,000 eV, Z = 1-92’, *Atomic Data and Nuclear Data Tables*, vol. 54, no. 2, pp. 181–342, Jul. 1993, doi: 10.1006/adnd.1993.1013.

[83] D. Paganin, S. C. Mayo, T. E. Gureyev, P. R. Miller, and S. W. Wilkins, ‘Simultaneous phase and amplitude extraction from a single defocused image of a homogeneous object’, *Journal of Microscopy*, vol. 206, no. 1, pp. 33–40, 2002, doi: 10.1046/j.1365-2818.2002.01010.x.

[84] J.-Y. Buffiere *et al.*, ‘In Situ Experiments with X ray Tomography: An Attractive Tool for Experimental Mechanics’, *Experimental Mechanics*, vol. 50, pp. 289–305, 2010, doi: 10.1007/s11340-010-9333-7.